Experimental quantification of the seismoelectric transfer function and its dependence on conductivity and saturation in loose sand

Julia Holzhauer, Daniel Brito, Clarisse Bordes, Yèble Brun, Bertrand Guatarbes

To cite this version:

Julia Holzhauer, Daniel Brito, Clarisse Bordes, Yèble Brun, Bertrand Guatarbes. Experimental quantification of the seismoelectric transfer function and its dependence on conductivity and saturation in loose sand. Geophysical Prospecting, 2016, 000, pp.0 - 0. 10.1111/1365-2478.12448 . hal-01386943

HAL Id: hal-01386943
https://hal.science/hal-01386943v1

Submitted on 24 Oct 2016

Geophysical Prospecting (0000) **000**, 000–000

Experimental quantification of the seismoelectric transfer function and its dependence on conductivity and saturation in loose sand

J. Holzhauer, D. Brito, C. Bordes, Y. Brun and B. Guatarbes
Univ. Pau & Pays Adour, CNRS, TOTAL - UMR 5150 - LFC-R
Laboratoire des Fluides Complexes et leurs Réservoirs
BP 1155 - PAU, F-64013, France

julia.holzhauer@univ-pau.fr,
daniel.brito@univ-pau.fr,
clarisse.bordes@univ-pau.fr,
yeble.brun@univ-pau.fr,
bertrand.guatarbes@univ-pau.fr

24 October 2016

SUMMARY

Under certain circumstances, seismic propagation within porous media may be associated to a conversion of mechanical into electromagnetical energy known as a seismoelectromagnetic phenomemon. The propagation of fast compressional P-waves is more specifically associated to manifestations of a seismoelectric field linked to fluid flow within the pores. The analysis of seismoelectric phenomena, which requires combining the theory of electrokinetics to Biot's theory of poroelasticity, provides us with a transfer function noted $E/\ddot{u}$ that links the coseismic seismoelectric field E to the seismic acceleration $\ddot{u}$. In order to measure the transfer function, we have developed an experimental set-up enabling seismoelectric laboratory observation in unconsolidated quartz sand within the kilohertz range. The investigation focused on the impact of fluid conductivity and water saturation over the coseismic seismoelectric field. During the experiment, special attention was given to the accuracy of electric field measurements. We concluded that, in order to obtain a reliable estimate of the electric field amplitude, the dipole from which the potential differences are measured should be of much smaller length than the wavelength of the propagating seismic field. Time-lapse monitoring of the seismic velocities and seismoelectric transfer functions were performed during imbibition and drainage experiments. In all cases, the quantitative analysis of the seismoelectric transfer function $E/\ddot{u}$ was in good agreement with theoretical predictions. While investigating saturation variations from the residual water saturation to full saturation, we showed that the $E/\ddot{u}$ ratio undergoes a switch in polarity at a particular saturation S^*, also implying a sign change of the filtration, traducing a reversal of the relative fluid displacement with respect to the frame. This sign change at critical saturation S^* stresses a particular behaviour of the poroelastic medium: the dropping of the coseismic electric field to zero traduces the absence of relative pore/fluid displacements representative of a Biot dynamically compatible medium. We concluded from our experimental study in loose sand that measurements of the coseismic seismoelectric coupling may provide information on fluid distribution within the pores, and that the reversal of the seismoelectric field may be used as an indicator of the dynamically compatible state of the medium.

Key words: Seismics, Monitoring, Reservoir Geophysics, Acoustics, Electromagnetics

1 INTRODUCTION

Seismoelectromagnetic effects may be observed when a seismic wave propagates within a porous medium formed from a solid frame filled with a fluid of low to moderate electrical conductivity.Under such conditions, an electrical double layer forms at the mineral-solution interface due to cations adsorption, thus enabling the setting of an electrokinetic coupling. The mechanically driven movements of the electrolyte relatively to the frame consequently result in a charge separation, producing a propagating electromagnetic (EM) field said to be "coseismic". According to the nature of the original seismic excitation, the propagating coseismic field may be overwhelmingly electric or magnetic; P-waves for instance are usually associated to coseismic seismoelectric (SE) fields. In any cases, seismoelectromagnetic manifestations will propagate similarly to the supporting seismic wave and will be affected by the properties - of either hydraulic, mechanical or electrical nature - characterizing the medium in its close vicinity. When the incident acoustic wave meets a discontinuity affecting the pore space in any geometrical or chemical manner (should it be a change in matrix density or a brutal variation of fluid conductivity), seismoelectromagnetic effects of a second kind, referred to as "interfacial" and propagating at EM-speed, might be generated. Such effects have been reported at field scale (Haines et al. 2007; Dupuis et al. 2007) and mesoscopic scale (Jougnot et al. 2013; Monachesi et al. 2015; Grobbe & Slob 2016). Note that as any physical coupling, seismoelectrics has a counter-effect known as electroosmosis, in which the application of an EM field induces a seismic propagation within a porous medium (Jouniaux & Zyserman 2016). This phenomenon was first reproduced at field-scale by Thompson & Gist (1993) before being observed at lab-scale by Zhu et al. (1999).

The possibility of combining seismic and electric surveys (electric field monitoring during seismic excitation) has been addressed as early as the 1930s. Following observations by Blau & Statham (1936), Thompson (1936) suggested using their combination as an exploration tool (producing what he refers to as the seismic-electric effect). A few years later Ivanov (1939, 1940), having run similar experiments in the field, suspected the observed signals to result from an electrokinetic coupling effect that he called seismic-electric effect of the second kind in distinction to piezoelectricity.

Frenkel (1944), attempted to develop a quantitative theory to explain Ivanov's observations. He formulated the first complete set of equations governing the acoustics of isotropic porous media. Yet it was Biot who, a decade later, achieved the first fully valid theory of poroelasticity. Biot (1956a,b) divided his treatment of the linear theory of porous media acoustics into two distinct frequency-domains, delimited with regard to the validity of Poiseuille flow assumption by introducing the Biot critical frequency f_{Biot}. He stated the existence of one rotational ($S-type$) and two dilatational ($P-type$) waves, subsequently referred to as $P-fast$ and $P-slow$, the latter being highly dispersive and diffusive. In a later paper Biot (1962) would emphasize the role this slow wave could play in electrokinetics, as it enhances fluid velocity within the pores. The next theoretical step to couple Biot's theory with electrokinetics while accounting for Onsager's reciprocity was taken by Neev & Yeatts (1989). Yet, in accordance with Frenkel's approach, they did not consider the full set of Maxwell's equation, leading them to ignore seismomagnetic effect. The breakthrough of seismoelectromagnetics was finally enabled by Pride's formulation of the underlying theory.

The theoretical background for seismoelectromagnetic phenomena was proposed by Pride (1994) as a set of equations based on Biot's original theory including the electrokinetic coupling as well as Maxwell's equations. In the light of this complete theory, the first dynamic transfer functions for the coseismic seismoelectric field were proposed a few years later by Pride & Haartsen (1996) for both transverse and longitudinal waves. Using low-frequency assumptions, Garambois & Dietrich (2001) proposed a linear expression linking the coseismic electric field to seismic acceleration of P-waves, applicable in particular to field measurements at seismic frequencies. Lately, seismic interferometry methods using Green functions (Wapenaar et al. 2006; Wapenaar & Fokkema 2006; Slob & Wapenaar 2007) have been adapted to provide the impulsive seismoelectric response of the porous medium equivalent to usual transfer functions. This method was first implemented for interfacial (Wapenaar et al. 2008; De Ridder et al. 2009) and coseismic (Schoemaker et al. 2012) seismoelectric before being extended by Gao & Hu (2010) to the seismomagnetic aspects.

Pride's theory being originally formulated for a fully-saturated porous medium, its adaptation to partially saturated conditions constitutes an important development offering new perspectives. While Biot's poroelasticity relations may be adjusted by defining effective fluid properties (Wood 1955; Teja & Rice 1981; Brie et al. 1995), saturation-dependence of electrokinetics is still discussed. It has been the subject of numerous theoretical developments initially proposed for the continuous spontaneous potential, some based on volume-averaging methods (Linde et al. 2007; Revil et al. 2007) others on capillary models (Jackson 2008, 2010), the former highlighting the role of the electrolyte wettability while the latter focuses on the thickness of the electrical double layer. Yet, to account for experimental observations, further empirical laws are often required (Guichet et al. 2003; Allègre et al. 2012). Eventually, the question of partial saturation has been directly broached under a seismoelectric angle either based on Pride's classical approach (Warden et al. 2013), or on an alternative reformulation using electrokinetic couplings as a function of charge density (Revil & Jardani 2010; Revil & Mahardika 2013; Revil et al. 2013).

The first seismoelectric laboratory experiments dealt with the impact of fluid properties on seismoelectric observations (Parkhomenko et al. 1964; Parkhomenko 1971; Parkhomenko & Gaskarov 1971). These types of laboratory experiments were eventually resumed by Ageeva et al. (1999) who introduced additional frequency variations. They observed at various frequencies that the ratio of the electric field to the liquid-phase pressure changed directly with water content and residual saturation on the one hand, and inversely with salinity, porosity and permeability on the other. In the meanwhile, an innovative laboratory apparatus of borehole geometry, involving Stoneley waves, enabled to observe coseismic and interfacial seismoelectric signals as well as electroosmosis (Zhu et al. 1999). On their borehole laboratory model, Zhu & Toksöz (2005) finally reported the observation of seismomagnetic coseismic signals using a Hall-effect sensor. Contemporaneously, quantitative measurements led by Bordes (2005) in an underground low-noise laboratory confirmed experimentally the existence of the coseismic seismomagnetic field and its dependence on shear-waves, as predicted by Pride's theory (Bordes et al. 2006, 2008).

After Zhu et al. (2000) and Zhu & Toksöz (2003) had investigated experimentally the dependence of coseismic electric amplitudes to fluid conductivity, Block & Harris (2006) confirmed the expected tendency of electric amplitudes to diminish with increasing conductivity on a sand column experiment. Finally Zhu & Toksöz (2013) conducted extensive and quantitative dynamic measurements of seismoelectric coupling coefficients under varying conductivities ($0.1 - 0.3\ S \cdot m^{-1}$): the seismoelectric coupling would decrease with increasing conductivity and increasing frequency. According to recent extensive measurements by Bordes et al. (2015) regarding the dependence of the coseismic seismoelectric signal on water saturation within the range $[0.3 - 0.9]$, the seismoelectric ratio $E/\ddot{u}$ showed a rather stable behaviour, despite large saturation changes expected to induce correspondingly large variations of the medium bulk conductivity.

Hence, in spite of its electrokinetic nature, seismoelectric effects have generally been expected to show some aptitudes for hydraulic characterization of porous media (Revil et al. 2015). Consequently, as part of the developing geophysical methods, seismoelectrics may eventually become a tool for reservoir characterization combining seismic and electric imaging abilities. Such perspective requires a comprehensive understanding of the underlying phenomena and their dependence to the involved medium parameters, as well as the preliminary development of a reliable quantitative measuring procedure. With this prospect, the goal of the present study is to perform quantitative measurements of the coseismic seismoelectric field for comparison to theoretical predictions, that is the study of the dynamic transfer function $E/\ddot{u}$.

Following the fundamental studies by Pride (1994) and Pride & Haartsen (1996), developments by Warden et al. (2013) and Bordes et al. (2015) extended the original formulation of the seismoelectric dynamic transfer function, initially written for saturated media, to partially saturated states. This step was taken by introducing the model for electrokinetic coupling dependence on saturation developed by Jackson (2010), along with a mechanical characterization of the biphasic fluid as a bulk effective fluid (the first topic has been discussed by Bordes et al. (2015), while the second will be more largely exposed in this article). This led to the relation between the acceleration $\ddot{u}$ due to fast P-waves, and its associated coseismic electric field E:

$$\frac{E}{\ddot{u}}(\omega, S_w, \sigma_f, \ldots) = i\,\frac{\tilde{\rho}L}{\omega\tilde{\epsilon}}\;\frac{Hs^2 - \rho}{Cs^2 - \rho_f} \qquad (1)$$

where ω is the angular frequency, S_w is the water saturation, σ_f is the fluid conductivity, $\tilde{\rho}$ is the effective density, L is the dynamic seismoelectric coupling coefficient, $\tilde{\epsilon}$ is the effective electric permittivity, H and C are poroelastic moduli of the medium, s is the slowness of the fast compressional P-wave, ρ is the bulk density of the porous medium and ρ_f is the effective fluid density. For the sake of clarity, the parameters dependence as a function of $(\omega,\, S_w, \ldots)$ is not explicitly written on the right hand side of eq. (1). Note that the original seismoelectric transfer function and the electrokinetic adjustment to partial saturation resulting in eq. (1) were both based on the assumption of an electrical double layer much thinner than the pore section (Pride 1994).

As detailed in Bordes et al. (2015), we considered the frequency-dependent transfer function $E/\ddot{u}$ as expressed in eq. (1) to depend on several parameters of the medium: some of them are related to the fluid phase, others depend on the solid phase and finally further parameters characterize the frame. Our present purpose is to quantitatively evaluate $E/\ddot{u}$ in a medium where the parameters can be inferred, either from direct experimental measurements or from theoretical estimations. We have therefore chosen to develop a metric sandbox experiment after initial works by Barrière et al. (2012) and Bordes et al. (2015). With its moderate propagation velocity under sub-saturated conditions and a granular matrix easily described by models, unconsolidated quartz sand appears particularly adapted to our purpose (Holzhauer 2015). Yet, from a practical point of view, wavelengths being decimetric in sub-saturated sand will grow metric in a fully-saturated medium. The characteristics of the experiment, as well as the physical properties of the sand are described in Part 2.

With all parameters of the medium involved in eq. (1) being reasonably known, our quantification attempt of the coseismic seismoelectric transfer function further requires high accuracy in acceleration $\ddot{u}$ and electric field E measurements at any given point of the sandbox. In this prospect, we have used calibrated accelerometers, and combined their results to those obtained on appropriately reconstructed dipoles which geometry is described in Part 3. Good knowledge of the sand physical parameters coupled to a reliable measurements routine will provides us with a precise estimation of the ratio $E/\ddot{u}$ for a given set of parameters during an experiment.

In order to validate our experimental approach in Part 4, we compare our measurements to theoretical predictions while varying the fluid conductivity σ_f, a key parameter for the amplitude of $E/\ddot{u}$, the other parameters remaining roughly constant throughout the experiments. Having concluded to the agreement between measurements and model predictions, we vary a more challenging parameter regarding experimental conditions, namely water saturation S_w. Related imbibition and drainage experiments are reported in Part 5. Part 6 eventually summarizes our results and concludes on our quantitative approach of the dynamic transfer function.

2 A MONITORED SEISMOELECTRIC EXPERIMENT

2.1 Description of the global set-up

We conceived a cubic sandbox from sealed plywood elements; a hole disposed on one side of the box allows the punch of a pneumatic seismic source to pass through. The inside is accessible by the open top. We arranged 3 cm-thick acoustic foam slabs at the bottom as well as on the opposed and lateral walls to the source in order to prevent boundary reflection effects. The dimension of the sandbox is $53 \times 50 \, cm^2$. It is filled with a 50 cm high sand-layer; the emission point of the seismic source is located at the center of a $50 \times 50 \, cm^2$ panel. Four injection wells placed at each corner of the sandbox allow for bottom imbibition. These wells are connected to elevated water barrels in an attempt to improve saturation degree by an increased water column. The average quantity of water required for initial imbibition would range by 60 liters. A global view of the experiment is given in Fig. 1a).

[Figure 1 about here.]

Since preliminary seismoelectric measurements demonstrated that the coseismic seismoelectric E field would be barely assessable for offsets much larger than 20 cm, all our captors were placed within a distance of 30 cm to the source. By this choice of offsets, we notably differed from previous seismic (Barrière et al. 2012) and seismoelectric (Bordes et al. 2015) laboratory analysis. While enabling high captor density (20 accelerometers within a maximal distance of 30 cm to the source), this receiver distribution required disposing the transducers on two parallel lines. A thin central space, aligned with the source, was left free to host an electrode array of 30 electrodes created in agreement with the specific offset-requirements. On this central line, electrodes were placed between offsets of 3 cm and 30 cm. Accelerometers were implanted on either side of this central line with a centimetric lateral offset as sketched in Fig. 2. Each accelerometer was systematically placed in regard to an electrode (see Fig. 1b) and Fig. 2). The sandbox was further equipped with moisture sensors surrounding the measurement line, with the purpose of recollecting saturation information.

[Figure 2 about here.]

2.2 The porous medium

The loose sand we used in our experiment is the same material as the one presented in the studies by Barrière et al. (2012) and Bordes et al. (2015): namely pure silica sand (SiO_2 content superior to 98%) showing unidisperse granulometry of 250 μm and grain density around $2635 - 2660 \, kg \cdot m^{-3}$. While hydraulic properties (as porosity, formation factor and permeability) were directly measured on small sand probes, other parameters, of electrical or mechanical nature, have been inferred from models or previous studies. The whole set of parameters and properties used in the present study is listed in Table 1 and follows the notations defined in appendices A and B from Bordes et al. (2015).

We estimated the zeta potential ζ, a parameter characterizing the electrical double layer, by extrapolating an experimental observation while using a ζ model depending on concentration C_0. On the one hand, Pride & Morgan (1991) showed the dependence of $\zeta \; vs \; log(C_0)$ to be linear, referring to various laboratory measurements in quartz sands. We then noticed that the slopes obtained from the different datasets were close to an averaged value of about $0.026 \, mV.l.mol^{-1}$ whereas the $\zeta(0)$ seemed to be a specific property of the medium. On the other hand, measurements by Nazarova-Cherrière (2014) showed the zeta potential in saturated Landes sand to be $\zeta = -35 \, mV$ (NaCl electrolyte, $\sigma_f \simeq 8.8 \, mS.m^{-1}$). Eventually, we used the relation $\zeta(C_0) = 0.044 + 0.026 \, logC_0$ (in mV) obtained by combining both model and measurements (see Table 1 for details).

[Table 1 about here.]

2.3 Pneumatic seismic source

The home-made pneumatic source was specifically designed to investigate the frequency range for which the medium should be most affected by Biot's losses, corresponding to the vicinity of the Biot frequency:

$$f_{Biot} = \frac{\phi \eta_f}{2\pi \gamma_0 \rho_f k_0} \tag{2}$$

estimated at approximately 2 kHz under sub-saturated conditions. In eq. (2) ϕ, γ_0, k_0 are respectively the porosity, the tortuosity and the permeability of the porous medium, while η_f and ρ_f stand correspondingly for the viscosity and density of the effective fluid. This source was made of a piston supplied with compressed air for one part, and a fixed frame that maintains the steel hitting plate by four screws equipped with shock-absorbers for another part (see Fig. 1a) and 1b)). The hitting punch showed by 0.5 cm within the box through the hole arranged on one side of the sandbox to transmit the impulsion from the pneumatic source to the medium. As an example of typical accelerations measured at the hitting plate (usually ranging from $1 \, km \cdot s^{-2}$ up to $5 \, km \cdot s^{-2}$), Fig. 3 shows a seismic record, yet only remotely indicative of the energy transmitted to the sand. This figure also demonstrates the excellent reproducibility of the seismic source during a given experiment, for which the stack of 25 consecutive pulses remains extremely close to the signal generated by one single shot. In Fig. 3b) we may also appreciate the wide frequency spectrum content of the pneumatic source around the kilohertz. The resonance frequency, observed at the source in both time and frequency records at approximately 19 kHz, is related to a characteristic frequency of the source system; that high-frequency component is not observed on the accelerometers buried within the sand. The original impulse in Fig. 3, filtered by a low-frequency Butterworth filter of degree 8 and cutoff frequency 25 kHz that eliminates the high frequency component, offers a more realistic view of the signal efficiently propagating within the sand.

[Figure 3 about here.]

2.4 Accelerometers, electrode array and moisture sensors

Our experiments involved two distinct types of accelerometers. A single DJB accelerometer of sensitivity $1 \, mV \cdot m^{-1} \cdot s^2$ (type $A/124/E$), was glued to the punching plate in order to measure accelerations at the source. *Brüel & Kjær* IEPE accelerometers of type "$4513 - 001$" and "$4513 - 002$" (1.27 cm diameter and a 1.56 cm length) were used for the sandbox instrumentation. These accelerometers claim average sensitivity of respectively $10 \, mV \cdot m^{-1} \cdot s^2$ and $50 \, mV \cdot m^{-1} \cdot s^2$ within the $[0.1 - 10 \, kHz]$ frequency range.

In our attempt to compare coseismic electric data to their corresponding seismic arrivals, special attention was given to spacial precision for measurements of both types. This concern steered the conception of a suitable electrode array, designed to improve precision on electric measurement localisation. This array was assembled from 30 stainless steel rods of equal length, acting as electrodes. In conformity with previous field-scale seismoelectric studies using stainless steel electrodes (Beamish 1999; Strahser et al. 2007, 2011), we verified that polarisation effects did not affect seismoelectric measurements. Control measurements conducted at similar fluid conductivity and saturation degree within a one-week interval, showed that we did not experience noticeable drift of the electric field, thus validating our choice of electrodes.

In order to keep the terminal connections out of the medium, chosen rods were of 50 cm length. Rigidifying units for the electrode array were kept away from the measurement plane to avoid the apparition of any guided waves. Each rod was then covered with a heat shrink tube on its whole length except for 0.5 cm at each of its ends, one end being the measuring tip while the other authorized the electric potential to be transmitted to the acquisition device. We decided to record each potential difference relatively to the furthest electrode of the array taken as a common reference (see the difference in electric potential measurement $V_i - V_{ref}$ in Fig. 2); this procedure validated by Bordes (2005), would ultimately facilitate the reconstruction of dipoles of any given length. We took the smallest electrode inter-trace we could manage in order to allow for very small dipoles, the smallest dipole-length being here of 0.9 cm. Finally, the relative position of accelerometers and electrode was anticipated as to match the offset of each accelerometer either with the center or with the tip of an electric dipole.

Accelerometers length being of 1.56 cm, we spaced our accelerometers by 3.6 cm and implanted them on either side of the central line with a lateral offset of 1 cm (see Fig. 2). The electrode array of length 27 cm, was surrounded by 7 water sensors, 2 of them arranged vertically at the middle of the horizontal planes located 10 cm beneath and 10 cm above the measuring plane, while 5 further captors were disposed within the measuring plane at a distance of approximately 10 cm from the measuring line, as indicated in Fig. 2. These captors, acting as capacitance probes, are sensitive to the dielectric permittivity of the surrounding medium on a volume of approximately 12 cm^3 with a precision of ± 3 to ± 5 %. The sensors have been calibrated for unconsolidated Landes sand; calibration methodology can be found in Barrière (2011). Finally, in our experiments, water saturation values S_w were obtained by averaging the synchronous measurements of the 7 water moisture probes.

2.5 The acquisition chain

The acquisition chain was composed of a dynamic signal acquisition device providing 32 simultaneous 24-bits analog inputs, 13 channels being dedicated to seismic recording while the remaining 19 channels were reserved for electric measurements. Electric recording procedure was completed by a home-made preamplifier of input impedance 1 $G\Omega$, meant to enable reliable measurements of electric potentials. This preamplifier also applied a high-pass filter cutting the recordings at 10 Hz. Saturation information were recorded thanks to an auxiliary device.

3 MEASURING ACCURATELY THE COSEISMIC ELECTRIC FIELD

3.1 General points and assumptions on the electric field

In coseismic seismoelectric field studies, we are dealing with a transient electric field, propagating concomitantly to its seismic support. In our experiments we consider the usual electric measurement derived from a potential difference between two points, upon the relation $\mathbf{E} = -\nabla V$ where $\mathbf{E}$ is the vectorial electric field and V is the electric potential. Thus, ΔV_{ij} is measured between two electrodes e_i and e_j as $\Delta V_{ij} = (V_i - V_{ref}) - (V_j - V_{ref}) = V_i - V_j$, forming the so-called dipole, the potential at each point being measured with respect to common reference V_{ref} (see Fig. 2). ΔV_{ij} is then divided by the dipole-length l_{dip} to retrieve the electric field according to the relation:

$$E_{ij} = -\Delta V_{ij}/l_{dip}. \quad (3)$$

Our experiment was precisely designed to investigate the stability of electric field measurements obtained from potential differences. During the experiments, potentials V_i were measured as a function of time at each electrode with respect to the common electrode. While electric acquisitions relatively to a common reference enabled us to reconstruct dipoles of any possible length, supernumerary electrodes offered the chance to translate a dipole of given length relatively to its corresponding accelerometer. In order to identify which dipole geometry was most appropriate as to accurately quantify the electric field at any given point, we checked the characteristics of the measured electric potential difference ΔV at a given point against some characteristics of the inducing seismic field. Due to the coseismic origin of the seismoelectric field (eq. (1)), and the linear relation of E to the potential (eq. (3)), it is expected that:

- the first signal in electric records should coincide in time with the first arrival in corresponding seismic records;
- the frequency contents characterizing seismic and seismoelectric fields should be relatively close, since dynamic effects are negligible within the kilohertz range (Bordes et al. 2015);
- the amplitude of the reconstructed electric field at any given point of the medium should ideally not depend on the selected dipole-length.

3.2 Effect of dipole geometry on electric potential waveform

The effect of dipole geometry on the measurement of seismoelectric fields has been a pending issue ever since this phenomenon regained attention in the 90's. Various authors (Beamish 1999; Strahser et al. 2007) investigated, at a given point, what influence the spacial distribution of electrodes may have on the estimate of electric field amplitudes. Regarding our experiment, we investigated the potential differences measured for two distinct dipole geometries as represented in Fig. 4a) and 4b) for the electrode $e_{5.8\ cm}$ located at offset 5.8 cm: the electrode array allows to investigate both the effect of dipole-length and dipole geometry relatively to the associated accelerometer located also at offset 5.8 cm. We have distinguished two cases of dipole reconstructions: in Fig. 4a) dipoles involving common mid-point geometry ΔV_M (reconstructed symmetrically to the mid-point electrode $e_{5.8\ cm}$) and in Fig. 4b) dipoles involving common first electrode ΔV_F (all dipoles having the electrode $e_{5.8\ cm}$ as their first electrode). Dipoles associated to ΔV_M and ΔV_F are then varied in length according to the value of l_{dip}.

Raw measurements of electric potentials ΔV_M and ΔV_F given by both dipole geometries of varying lengths are compared respectively in Fig. 4c) and 4d) where the electric potentials are represented as a function of time at offset $5.8\ cm$. For the common mid-point geometry, both the voltage and the time location of the maxima are highly dependent on dipole-length as seen in Fig. 4c). In this aspect, the electric signal behaves as expected since the larger the mid-point dipole we consider, the closer to the seismic source the first electrode will be. Conversely, for the first-electrode geometry in Fig. 4d), we note that the envelope of the first electric signal evolves significantly in shape and in amplitude only as the dipole-length l_{dip} increases from $0.9\ cm$ to $2.7\ cm$. For $l_{dip} \geq 2.7\ cm$ the waveform of the first electric arrival remains very similar.

In Fig. 4e) and 4f), we considered the same records as in 4c) and 4d) and compared them to their seismic counterpart $\ddot{u}$ measured at the middle location of the dipole (common mid-point geometry) or at the first electrode (first-electrode geometry), their locations corresponding both to offset $5.8\ cm$. In this representation, seismic and electric signals are both normalized to 1 at the location of their respective maximum as to facilitate their comparison. It appears clearly that the best agreement in arrival-time for seismic and electric signals is found for the common mid-point geometry, shown in Fig. 4e). Regarding the frequency content, the shorter the dipole length l_{dip}, the closer the electric waveform will be to that of the seismic first arrival for both common mid-point and first-electrode geometries (see Fig. 4e) and 4f) respectively.)

[Figure 4 about here.]

3.3 Role of dipole-length with relation to dominant seismic wavelength

In order to generalize to all offsets the observations performed at offset $5.8\ cm$ in Fig. 4, we focused on a chosen experiment performed at $S_w = 0.94$ and $\sigma_f = 2.5\ mS \cdot m^{-1}$ from which we systematically picked the first maximum in electric records $\Delta V_{M,F}$ for offsets within [$3\ cm$ - $11.2\ cm$] and for reconstructed dipole lengths $0.9\ cm \leq l_{dip} \leq 11.2\ cm$. We then expressed l_{dip} relatively to a local wavelength value $\lambda = V_p/f_{nom}$ estimated from the seismic first-arrival velocity V_P, and from the central frequency f_{nom} of the first seismic arrival. The averaged wavelengths λ for our sub-saturated experiments is approximately of $17\ \pm 3\ cm$.

Results for the mid-point dipole geometry are shown on the left column in Fig. 5a), 5c) and 5e). As previously observed at offset $5.8\ cm$ in Fig. 4c), the maximum of the electric potential ΔV_M increases nearly as a function of the dipole length l_{dip}/λ for all offsets. The electric field $|E_M|$ in Fig. 5c) derived from ΔV_M in Fig. 5a) seems to be relatively constant as a function of l_{dip}/λ for all offsets, meaning eq. (3) is well-satisfied. Hence, the mid-point dipole geometry appears suitable to derive a stable electric field at any given point. Finally, in Fig. 5e), we first picked the time for the maximum amplitude of the electric and the seismic signals respectively, and then represented the ratio $t_{max}(\Delta V)/t_{max}(\ddot{u})$. Since the electric field is supposed to be coseismic, $t_{max}(\Delta V)/t_{max}(\ddot{u})$ should be very close to a value of 1. It appears in Fig. 5e) that if one wants to study a pure coseismic electric field, $i.e.$ electric and seismic time records evolving in phase, then one must favour mid-point electric dipole of length $l_{dip}/\lambda \leq 1/5$.

Distinctly, the same approach on first-electrode geometry in Fig. 5b), 5d) and 5f) leads to different conclusions. ΔV_F in Fig. 5b) first increases linearly as a function of l_{dip}/λ before reaching a plateau for $l_{dip} \geq \lambda/5$. In both cases, the derived electric field $|E_F|$ in Fig. 5d) strongly varies as a function of l_{dip}/λ, for all considered offsets. Finally, Fig. 5f) demonstrates that the first-electrode geometry is not best suited to obtain an electric field coinciding in time with the seismic field, since $t_{max}(\Delta V)/t_{max}(\ddot{u})$ differs noticeably from 1 at any given offset and for any dipole-length.

[Figure 5 about here.]

3.4 Definition of the reference dipole geometry

To conclude on the most appropriate dipole for punctual electric field measurement in our experimental set-up, we compiled the electric field derived from the maxima in potential differences obtained over a variety of experiments in the first-electrode configuration with $l_{dip} = 0.9\ cm$ (smallest in the experiment) and in the mid-point dipole case with $l_{dip} = 1.8\ cm$ (being the smallest of its sort as well). In Fig. 6, the experimental data points remarkably align along the identity slope over two orders of magnitude of electric field variations. It supports the idea that, with regards to the sole amplitude of the electric field at any given point, it is equivalent to use the first-electrode dipole or the common mid-point dipole as long as we remain within the range of very limited dipole-lengths.

[Figure 6 about here.]

We conclude that the best match between seismic and seismo-electric waveforms is obtained for relatively small dipole-lengths of any geometry conforming with $l_{dip} \leq \lambda/5$. Yet characteristic arrival-times in seismic signals are in better agreement with those observed for the smallest mid-point dipoles rather than for the smallest first-electrode dipole. We accordingly choose to consider the common mid-point geometry. As a consequence, for the rest of our investigations the electric field will be determined on the smallest mid-point dipole, $i.e.$ a dipole of length $1.8\ cm$ and of mid-point geometry.

4 EFFECT OF FLUID CONDUCTIVITY ON TRANSFER FUNCTIONS

A sensitivity analysis performed over the various mechanical, electrical and hydraulic properties of the medium showed that one of the most important effect on the amplitude of the dynamic seismoelectric transfer function presented in eq. (1), $|E/\ddot{u}(\omega, S_w, \sigma_f, \ldots)|$, was produced by a change in fluid conductivity (Holzhauer 2015). Transfer functions $|E/\ddot{u}(S_w, \omega)|$ obtained for a saturation of $S_w = 0.95$ and three different conductivities σ_f are shown in Fig. 7 as a function of frequency, all other parameters of Table 1 remaining constant. As expected (Garambois & Dietrich 2001; Bordes et al. 2015) a low-frequency plateau is followed by a gradual decrease of the transfer function in the vicinity of the Biot frequency. Fig. 7 confirms that a slight change in fluid conductivity σ_f impacts significantly the amplitude of the transfer function.

[Figure 7 about here.]

The fluid conductivity also happens to be the most adjustable parameter within a sandbox experiment: as a fluid property, its change demands no great operation but to patiently equilibrate the medium towards the wanted conductivity value by continuous water circulation. In the following, we focus on measuring that seismoelectric transfer function during the experiments, in an attempt to characterize the variation of this function as fluid conductivity σ_f is changing.

As soon as the 70's, Parkhomenko & Gaskarov (1971) noted in their conclusions that "as the degree of mineralization of the solution saturating the rock increases, the magnitude of the E-effect is reduced approximately exponentially" for experiments conducted on partially saturated sand having NaCl conductivities ranging from 47 $mS \cdot m^{-1}$ to 19 $S \cdot m^{-1}$. This effect was particularly brought to light in the low-frequency approximation of the coseismic transfer function given by Garambois & Dietrich (2001), which proved the dependence of the coseismic transfer function to be inversely proportional to fluid conductivity. Within the last decade, further similar studies have been conducted either on sand and glass beads (Block & Harris 2006) or on Berea sandstone (Zhu & Toksöz 2013) for frequencies reaching some tens of kilohertz.

In our experiment, investigation of the transfer function dependence on fluid conductivity was conducted following initial imbibition. The medium was first equilibrated with demineralized water for a couple of hours, eventually giving the measurement at a lowest value of $\sigma_f = 1.7\ mS \cdot m^{-1}$. Fluid conductivity was then controlled by progressive addition of NaCl salts to eventually cover fluid conductivities ranging from 2.5 $mS \cdot m^{-1}$ to 10 $mS \cdot m^{-1}$. Throughout this process, the conductivity of the fluid was repeatedly measured with a conductimeter within the four injection wells at the corners of the sandbox; the homogeneity of the fluid conductivity within the box was verified by another measurement at the at the top of the sand layer. In Fig. 8, we present three acquisitions realized within some days after initial imbibition of the medium. Beside stacking, the sole treatment applied to these data consists in electric reconstruction of the 1.8 cm mid-point dipoles. Each electric record in Fig. 8 is compared to its synchronous seismic, both signals being scaled relatively to one another in order to be compared.

From the less to the most saline experiment, water saturation stayed within the 0.95 ± 0.02 range, the P-wave velocity ranging by $165 \pm 20\ m \cdot s^{-1}$. Some discrepancies remain however between the seismoelectric and seismic velocities, the latter being always slightly higher than the former when determined on first-arrival basis. Yet, the most interesting observation in Fig. 8 is that, while seismic remains mostly invariant in amplitudes throughout the experiments, electric amplitudes decrease drastically, almost by one order of magnitude, as fluid conductivity increases from $1.7\ mS \cdot m^{-1}$ to $7.7\ mS \cdot m^{-1}$. We also note that our experimental values of $|E/\ddot{u}|$ evolves as expected with respect to the fluid conductivity σ_f: as awaited the coseismic ratio decreases as conductivity increases.

[Figure 8 about here.]

Fig. 9 presents a comparison between the measured ratio $|E/\ddot{u}(S_w, \omega)|$ and the corresponding theoretical conductivity-dependent dynamic transfer function, computed after eq. (1). For a given conductivity, experimental $|E/\ddot{u}|$ values are shown at various offsets together with their corresponding averaged values and standard deviations. Like in Bordes et al. (2015), values of $|E/\ddot{u}|$ vary noticeably as a function of offsets, although these variations are not predicted from the theoretical expression of the coseismic electric field as presented in eq. (1). This dispersion of amplitude ratios might therefore be seen as an experimental bias, being eventually used for the estimation of uncertainties by standard deviation.

The frequency signature of the first seismic and electric signals being grossly encompassed within the $[0.5 - 2\ kHz]$ range, in Fig. 9 we represented the dynamic transfer function for these two bounding frequencies at a saturation $S_w = 0.95$. Although the error bars on experimental data are quite significant, the agreement between averaged experimental and theoretical points is convincing; in particular, the decreasing trend of $|E/\ddot{u}|\ vs\ \sigma_f$ is well-retrieved from experimental data.

We finally added to Fig. 9 an averaged value of the experimental transfer function measured in Bordes et al. (2015) at further offsets than in the present study, $i.e.$ at offsets of 20, 30 and 40 cm. These measurements were performed with first-electrode geometry and a value of $l_{dip}/\lambda \simeq 0.4$ (λ being the typical wavelength defined from the central frequency and apparent velocity of the seismic first arrival in time records). Based on previous study regarding the dipole lengths (Part 3), more specifically focusing on the first-electrode measurements shown in Fig 5 d), we can infer that the electric amplitude related to the point shown in Fig. 9 taken from Bordes et al. (2015) could be underestimated by a factor between 2 and 4. Based upon that correction, the point from Bordes et al. (2015) would match the trend of $|E/\ddot{u}|\ vs\ \sigma_f$ established in Fig. 9 of the present study .

[Figure 9 about here.]

As a conclusion, the mid-point geometry, when associated to very short dipoles, provides some $|E/\ddot{u}|$ measurements very close to theoretical predictions based on Pride's theory generalised to effective medium under partial saturation conditions. Eventually, the chosen dipole geometry seems to enable accurate and quantitative measurements of the transfer functions whatever the fluid conductivity.

5 THE ROLE OF WATER CONTENT ON COSEISMIC SEISMOELECTRIC TRANSFER FUNCTIONS: A FULL SATURATION RANGE ANALYSIS

5.1 Experimental observations

Part 4 having validated the use of eq. (1) to estimate the seismoelectric transfer function $|E/\ddot{u}|$ by varying one influent parameter σ_f, we now address its validity with respect to a further parameter of important impact: the water saturation degree S_w. Our study relies on three rounds of experiments during which saturation variations were closely monitored. These three rounds are represented in terms of measured P-wave velocities in Fig. 10. First, we acquired data related to an initial imbibition starting from dry sand: it provided us with seismic properties of the medium under dry and sub-saturated conditions. The medium was then put to a rest for one month, with occasional fluid re-equilibrations by water circulation. The achievement of full saturation launched the second round of experiments, consisting in a monitored drainage process from $S_w = 1$ to $S_w \simeq 0.3$ over 11 hours. The medium was subsequently submitted to a rapid and poorly documented cycle of imbibition-drainage, not reported here, in a failed attempt to re-reach immediate full saturation before the medium had rested long. Eventually, this failed attempt was followed by a third experimental round monitoring re-imbibition with progressive addition of water from the residual water saturation $S_{w0} \simeq 0.25$ to $S_w \simeq 0.9$.

[Figure 10 about here.]

A series of velocity values describing this set of three experiments is to be found in Fig. 10. These velocity values were estimated by linear regression on basis of first-arrival time-picking between offsets 10 to 23 cm. As a striking feature of Fig. 10, we note the hysteretic behaviour of the measured seismic velocities during the three experiments. Indeed, while low-saturation velocities for the drainage and secondary imbibition tend to superpose, they do not converge towards the initial dry sand velocity value preceding first imbibition. Similarly, for higher saturation degrees such as $S_w > 0.5$, drainage velocity values tend to be greater than those for imbibition at comparable saturation degrees. This type of behaviour has repeatedly been reported in literature, testifying of higher velocities while draining than while imbibing. Walton (1987) and Barrière et al. (2012) associated this phenomenon to a weakening of the frame when injecting fluid during imbibition. Alternatively, Knight & Nolen-Hoeksema (1990) and Cadoret et al. (1995) attributed this discrepancy to a homogeneity loss of the effective fluid (air+water) while drying, in comparison to the homogeneity level experienced during imbibition (often under depressurization). According to them, while fluid and gas can coexist within a pore during the imbibition phase and favour homogeneity of the medium, drainage would rather see that a pore is either filled with or emptied from its water, according to its aspect ratio. Characteristics of the effective fluid were indeed involved under the form of an adaptive effective fluid modulus K_f in the calculation of the corresponding velocity models presented as solid and dashed lines in Fig. 10 (respectively standing for the best fits and misfits of 10%). These models are resulting from least-square joint inversion of the $V_P(S_w)$ data in question, and their related saturation-dependent $E/\ddot{u}$ ratios (see Fig. 12 to come) in the context of the the partially saturated seismoelectric model presented in eq. (1); the models for effective-fluid-modulus description will be further explained in this last section.

The evolution of seismic and electric records with water saturation during the time-lapse monitored drainage, second of the three cycles of experiments, is now presented in Fig. 11. A sign inversion of the coseismic electric field with respect to the seismic acceleration was observed during that drainage. In our experimental data, while the seismic waveform evolves much with saturation, the first arrival remains always negative as recorded by accelerometers and as expected for an initial compression. On the contrary, the electric field appears to reverse its sign during the drainage course, leading to a sign inversion of the experimentally measured $E/\ddot{u}$.

Despite large errors due to a poor signal-to-noise ratio and a possible DC shift of the electric field with respect to the zero baseline, we could determine that the sign change happens for $S_w \simeq 0.6$ on observations made at offsets 3.9 cm and 5.8 cm. At further offsets ($> 5.8\ cm$) the limited number of available stacks (from 5 to 25), imposed by the time-lapse nature of the experiment, was unfortunately not sufficient to provide reliable information on the coseismic seismoelectric signals.

[Figure 11 about here.]

In order to gain some insights into the origin of the sign inversion of the dynamic transfer function, we focused on the sign of $E/\ddot{u}$ at offset 3.9 cm, that offset being the best-documented throughout the whole time-lapse monitored experiment. In Fig. 12, we consider all data associated to a saturation information (drainage or imbibition) by representing the $E/\ddot{u}$ ratio vs water saturation S_w. This compilation encompasses data acquired at various conductivities during initial imbibition, as well as data acquired at constant conductivity $\sigma_f = 7.2\ mS \cdot m^{-1}$ during the drainage phase and a following re-imbibition. In order to be studied relatively to their saturation dependence, $E/\ddot{u}$ ratios determined for initial imbibition, while varying conductivity σ_f, were rescaled into their expected values at 7.2 $mS{\cdot}m^{-1}$ by using eq. (1).

[Figure 12 about here.]

5.2 Determination of the effective fluid moduli and relation to homogeneity degree

Having determined $V_P\ vs\ S_w$ (Fig. 10 at offset 3.9 cm) and $E/\ddot{u}$ $vs\ S_w$ (Fig. 12) during the time-lapse monitored experiments, we intended to understand these measurements in the context of dynamic transfer functions under partial saturation conditions. First, we noticed that the velocity variations shown for the three cycles in Fig. 10, call for a necessary change in the properties of the effective fluid during the experiments, combined to a modification in the solid frame consolidation of the porous medium. These changes involve the incompressibility of the drained solid frame K_D and the effective fluid modulus model $K_f(S_w)$.

Concerning the bulk modulus K_D, the initial value of 25.5 MPa proposed by Barrière et al. (2012), deduced from Walton (1987) developments on grain-contact theory, is well-adapted to account for initial imbibition, for which low-saturation velocity plateau was estimated at $170 \pm 5\ m{\cdot}s^{-1}$, based on measured velocities at extreme saturation degrees $S_w = 0$ and $S_w = [0.9 - 0.95]$. For drainage and re-imbibition data, this well-monitored velocity has increased to $230 \pm 10\ m \cdot s^{-1}$. To reproduce such plateau value, bulk modulus K_D had to be increased to 50 MPa. A possible explanation to this increase between the initial imbibition and the following cycles could involve a consolidation process of the porous frame as residual water produces surface tension (Gallipoli et al. 2003).

Regarding the effective fluid modulus variations with saturation $K_f(S_w)$, we considered two models. The first model is the so-called Reuss average (Wood 1955), classically associated to isostress conditions (Mavko et al. 2003) and hence adapted to a homogeneous effective fluid:

$$\frac{1}{K_f(S_w)} = \frac{1}{K_R(S_w)} = \frac{1 - S_w}{K_g} + \frac{S_w}{K_w} \tag{4}$$

where K_w and K_g are respectively the liquid water-phase and gaseous air-phase elastic moduli (see Table 1). The Reuss model is particularly suited to well-homogenized porous media, for which heterogeneities are small in comparison to the wavelength. The second model, identified as the Brie model, is calculated as a saturation power-law of chosen exponent e (Brie et al. 1995):

$$K_f(S_w) = K_{B\ e}(S_w) = (K_w - K_g){S_w}^e + K_g \tag{5}$$

This adaptable empirical law has been used with moderate e exponent ($e \lesssim \mathcal{O}(10)$) to account for inhomogeneous fluid conditions: in this respect, a parallel to patchy saturation was drawn in Carcione et al. (2006) and Dvorkin et al. (1999), Brie's model offering the advantage of being very straightforward as its implementation requires no preliminary knowledge on patches size and distribution. Interestingly, we note that a Brie model with exponent $e = 1$ corresponds to the Voigt arithmetic average (Voigt 1928), particularly suited to characterize isostrain conditions (Mavko et al. 2003). It defines a upper bound for modulus of the multiphasic fluids, despite being poorly adapted to their description. High values of the e exponent on the other hand ($e \simeq \mathcal{O}(100)$) are best-suited to model homogeneous medium. Note that as e increases towards higher values, $K_{B\ e}(S_w)$ comes closer to the Reuss model $K_R(S_w)$ before eventually surpassing it.

We have tested Pride's model for velocity and seismoelectric transfer function using the Reuss definition for effective fluid modulus $K_R(S_w)$ coupled with the properties listed in Table 1. The results, mapped as black plain lines in Fig. 10 and Fig. 12, reveals that the cycle which is better described as an homogeneous effective fluid of Reuss type is the initial imbibition represented in both figures as blue data points. Using $K_D = 2.5 \times 10^7\ Pa$ (see Table 1), the Reuss model offers a fair estimate of our experimental velocities (Barrière et al. 2012). In Fig. 12 however, the $E/\ddot{u}$ data related to the first imbibition cycle are not that well-explained by the Reuss model.

In an attempt to gain more information on the homogeneity degree of the medium during these time-lapse monitored experiments realized in three periods, we inverted jointly seismic velocities V_P and local estimates of the coseismic seismoelectric transfer function $E/\ddot{u}$ respectively presented in Fig. 10 and Fig. 12. This least-square inversion was led in the theoretical context of the partial saturation model evoked in eq. (1). The inversion was run taking the Brie exponent e as the only free parameter, all further physical properties being given in Table 1. Results of the least-square inversion are presented in Fig. 10 and Fig. 12 for each monitored cycle. In those figures, each best-inverted solution (plain line) is bracketed by a couple of functions (dashed lines) giving solutions with a 10% error in the misfit function compared to the best solution. The inverted models, although failing in following precisely the data, seem to qualitatively account for the three types of behaviour encountered in V_P and $E/\ddot{u}$ during the three cycles. As a result, the inverted e exponent appeared much more sensitive to the $E/\ddot{u}$ data rather than to acceleration measurements; that high sensitivity to electric measurement is explained by the high variability of the $E/\ddot{u}$ function $vs\ S_w$ with respect to the variable exponent e, whereas the change of the V_P function $vs\ S_w$ with e are less important and consequently less discriminant regarding the inversion process.

The inversion of first imbibition data confirms a high homogeneity level of the medium during initial imbibition since the inverted exponent is $e = 61 \pm 11$. It is important however to stress that this inversion is rather poorly constrained given that the $E/\ddot{u}$ values were only measured at very high saturation S_w. A Brie exponent of $e = 9 \pm 2$ was obtained for the inversion regarding the drainage, that case being the most-constrained with the maximum of data in Fig. 10 and Fig. 12, resulting in a very small variation of the inverted exponent. The quite low value of the inverted e exponent reveals a relatively heterogeneous medium during drainage. The Brie model for the effective fluid modulus $K_f = K_{B9}$ fits the $E/\ddot{u}$ experimental data particularly well, inclusive of the sign inversion occurring around $S_w \simeq 0.6$. The inversion of the second imbibition data lead to an exponent $e = 32 \pm 5$, intermediate between the initial imbibition and the drainage, traducing an homogeneity increase of the effective fluid (Knight & Nolen-Hoeksema 1990; Cadoret et al. 1995), yet not as good as when starting from dry material. This might be due to the trapping of air bubbles within small pores during the refilling process. For this case corresponding to $e = 32$, the change in sign would be expected for a saturation degree approaching 0.9. Though we might identify an onset of this sign change when looking at experimental points over 0.8 saturation, we were never able to reach the saturation break point, despite how long we waited and how often we put the fluid to circulate.

5.3 Investigation on the origin of the sign change in $E/\ddot{u}$

Finally, the sign change of the transfer function visible in Fig. 12 was fully experienced only once during the drainage phase, while initial imbibition resulting in $S_w > 0.95$ offered strictly negative ratios and secondary imbibition jamming at $S_w = 0.88$ gave overwhelmingly positive ratios. We have investigated the origin of the sign change by considering eq. (1) as a function of S_w. This equation can also be rewritten as:

$$\frac{E}{\ddot{u}}(\omega, S_w, \sigma_f, \ldots) = \left(\frac{\tilde{\rho}L}{i\omega\tilde{\epsilon}}\right)\beta = -\left(\frac{\tilde{\rho}L}{i\omega\tilde{\epsilon}}\right)\left(\frac{H(S_w)s^2(S_w,\omega) - \rho(S_w)}{C(S_w)s^2(S_w,\omega) - \rho_f(S_w)}\right), \tag{6}$$

where the new β-term is a mechanical coupling related to the fluid/matrix displacement ratio (Pride & Haartsen 1996). That β-term of sheer mechanical origin is the only term to change sign as a function of saturation in eq. (6).
This change of sign occurs at a particular saturation S^* where, from eq. (6),

$$H(S^*)s^2(S^*,\omega) - \rho(S^*) = 0. \tag{7}$$

It means that the phase velocity of the fast P-wave should be:

$$V_P(S^*) = 1/s(S^*) = \sqrt{\frac{H(S^*)}{\rho(S^*)}}, \tag{8}$$

an expression valid at all frequencies, no frequency-dependence being observed.

Since $\beta = 0$ at S^*, there should be no fluid/matrix relative motion, and the energy dissipation of the "Biot" type induced by macroscopic fluid flow should vanish. In Fig. 13a), we computed the inverse of the seismic quality factor $Q^{-1}(S_w)$ with regard to the Reuss and Brie models for effective fluid modulus $K_f(S_w)$. As expected, for all curves Q^{-1} is put to zero at critical saturation S^*, thus confirming that dissipation and attenuation effects vanish at that particular point. The eventuality of such manifestations had been theoretically addressed by Hu et al. (2002) in the context of seismoelectrics. In their parametrical study, they considered a fully saturated porous medium of varying porosity and identified a porosity degree for which no mechanical losses were expected. That particular fluid/solid association was acknowledged as a dynamically compatible medium, as defined by Biot (1956a).

[Figure 13 about here.]

To complete our investigation on the origin of the sign change, we studied the relation between fluid and frame displacements (respectively u_f and u) within the porous medium. As defined by Pride (1994), the filtration $\mathbf{w} = \phi\ (\mathbf{u_f} - \mathbf{u})$ characterizes the relative motion between phases and is related to the frame displacement by $\mathbf{w} = -\beta\mathbf{u}$. Hence, the fluid and frame component of the displacements in the direction of the seismic propagation are linked by the relation:

$$\frac{u_f}{u} = 1 - \frac{\beta}{\phi}. \tag{9}$$

Fig. 13b) displays the u_f/u ratio $vs\ S_w$ for the same models as presented in Fig. 13a). Not surprisingly, u_f/u reaches unity at critical saturation S^*. At this point, u_f is strictly equal to u and the filtration disappears, the frame being displaced in phase with the fluid as the seismic wave propagates: neither attenuation, dispersion nor seismoelectromagnetic coupling can occur. For $S_w < S^*$, the fluid displacement is greater than the frame displacement induced by seismic wave propagation (u_f/u > 1 and w > 0); for $S_w > S^*$ instead, the absolute fluid displacement is shorter than that of the frame (u_f/u < 1 and w < 0). As the sign of the filtration term w determines the sign of the potential difference ΔV, it ultimately governs the sign of the dynamic transfer function $E/\ddot{u}$.

Although the singular value $S_w = S^*$ is observed distinctly through an electrokinetic measurement, the origin of the filtration reversal is to be found in mechanical properties. When we consider partially saturated sand, mechanical properties change indeed dramatically with S_w. In such medium, $K_D \ll K_S$ and the undrained modulus can be reasonably approximated by (Pride 2005):

$$K_U(S_w) \simeq K_D + \frac{K_f(S_w)}{\phi} \tag{10}$$

Hence, the P-wave modulus can be expressed as:

$$H(S_w) = K_U(S_w) + \frac{4}{3}G \simeq (K_D + \frac{4}{3}G) + \frac{K_f(S_w)}{\phi}. \tag{11}$$

From this equation, we define two P-wave moduli H_{fr} and H_f, respectively associated to the frame and fluid contributions:

$$H_{fr} = K_D + \frac{4}{3}G \qquad \text{and} \qquad H_f(S_w) = \frac{K_f(S_w)}{\phi}. \tag{12}$$

H, H_{fr} and $H_f(S_w)$ are computed $vs\ S_w$ in Fig. 13c) for only two of the models presented in Fig. 13a) and 13b), with the purpose of clarity. For the lowest saturation degrees, H is dominated by H_{fr} since the saturating fluid is mostly a very compressible gas. When saturation progressively increases, the modulus H_f increases as well, following the rapid evolution of $K_f(S_w)$ expressed by the Brie effective models in Fig. 13c). The critical saturations S^*, denoted as stars in Fig. 13, are always reached in close vicinity to a saturation degree where H_{fr} and H_f equally contribute to H. For larger saturation degrees, the P-wave modulus H is dominated by the fluid contribution H_f.

5.4 Results

Our analysis involving poromechanical moduli gives conclusive evidences about the origin of the polarity shift observed in seismoelectric transfer functions: the shift occurs at a critical saturation degree S^* marking a transition between two different mechanical regimes. The first regime, corresponding to relatively low water saturations, is characterized by a dominant incompressibility of the frame, implying a bigger displacement of the fluid with respect to the frame ($w > 0$) as the seismic wave propagates. Conversely, at relatively larger saturation degrees, the incompressibility of the fluid overtakes that of the frame, causing the frame displacement to become larger than that of the fluid ($w < 0$) as the seismic wavefront passes.

It is of importance to note that this change in polarity $E/\ddot{u}$ is very specific to unconsolidated porous media filled with gas-water mixture, combining a highly variable effective fluid modulus $K_f(S_w)$ with a very low frame modulus such as $K_D \ll K_S$. It would be hardly observable in a consolidated medium such as sandstone for which fluid and frame moduli monotonously verify $K_f(S_w) \ll K_D$. Nor would it occur in unconsolidated sand filled by an effective fluid such as an oil-water mixture, for which the fluid modulus would remain relatively stable while S_w varies. Despite these restrictions, our study offers an experimental evidence for what has been defined by Biot (1956a) as the "dynamic compatibility condition", which has long been considered as a theoretical object of study (Burridge & Vargas 1979; Simon et al. 1984; Mesgouez et al. 2005), yet had, to our knowledge, never been directly observed. Further questions remain as how to find a theoretical explanation unifying our observations with the projections from Hu et al. (2002), the first requiring partial saturation while the other assumed a fully saturated media. The answer stands possibly in relation to the thermodynamics of capillary pressure in porous media as developed by Wei & Muraleetharan (2002a,b).

6 CONCLUSION

The purpose of our study was to achieve high spatial and temporal resolution while measuring the seismoelectric coupling on a medium submitted to important changes in fluid conductivity and saturation, up to saturation completion. Special attention was given to acceleration and electric potential measurements in order to derive accurate estimations of the dynamic transfer function $E/\ddot{u}$. Experimental measurements, performed at frequencies in the kilohertz range, were compared to the theoretical framework for coseismic seismoelectric established by Pride (1994) and Pride & Haartsen (1996) and extended to partial saturation conditions by Warden et al. (2013) and Bordes et al. (2015).

The high-resolution electrode array placed in our sandbox led to convincing conclusions regarding the relevant dipole length l_{dip} for electric field measurements. We clearly showed that l_{dip} should necessarily be of maximum length $\lambda/5$, λ being the wavelength of the propagating seismic wave. Should this condition not be satisfied, the value of the local electric field derived as -$\Delta V/l_{dip}$ may be underestimated, thus impacting the transfer function determination. We also demonstrated that the best-suited dipole geometry for coseismic transfer function estimation should be centered on the point where the corresponding seismic acceleration is measured. A direct comparison of seismic and electric field waveforms showed that, for first-electrode dipole geometry, we may observe a tradeoff between seismic and electric arrival-times, although not altering the amplitudes of the electric voltage with respect to the seismic field. While these experimental results on dipole geometry are rather conclusive, a numerical study would be particularly relevant to test other possible geometries of electrodes ($e.g.$ multipoles) at laboratory and field scales.

From the theory, we expected fluid conductivity σ_f to have a strong impact on the amplitude of the seismoelectric transfer function. Therefore we performed a set of experiments under varying conductivities while all other parameters, in particular saturation degree S_w, remained fixed. We thus checked a well-established result that is the decrease of the seismoelectric transfer function $E/\ddot{u}$ as fluid conductivity increases. Quantitatively, the experimental points measured at saturation degrees close to $S_w \simeq 0.95$, for various conductivities, were quite remarkably predicted by the coseismic seismoelectric model at partial saturation involving the saturation-dependent electrokinetic coupling model of Jackson (2010). That positive agreement between experimental data and theory legitimated our further use of the transfer function adapted to partially saturated conditions under an effective fluid approach.

Saturation degree S_w being another key parameter, we monitored the same experimental set-up under varying water content and performed a full saturation range monitoring over a couple of imbibition and drainage sequences. The time-picking of seismic first arrivals led to hysteretic observations classical for unconsolidated media: seismic velocity values V_P from imbibition and drainage do not superpose, an effect we attributed to changing mechanical properties of the partially saturated sand. During those imbibition-drainage cycles, we simultaneously compiled the measurements of $E/\ddot{u}\ vs\ S_w$ taken at the closest offset to the source. We then proceeded to the joint inversion of the saturation-dependent V_P and $E/\ddot{u}$ values in the least-square sense on basis of eq. (1). The adjustable variable during this inversion was Brie's effective fluid modulus $K_{B\ e}$ through its exponent e, as it traduces the degree of homogeneity of the multiphasic fluid within the porous medium. The V_P and $E/\ddot{u}$ measurements were satisfactorily explained by the inversion, yet the inverted coefficient e seemed to be much better constrained by the electric data than by the velocity measurements. The first imbibition, starting from dry sand, appeared to be achieved under highly homogeneous fluid distribution as attested by the fitting effective modulus (high e exponent). On the contrary, the drainage revealed to be quite heterogeneous (low e exponent), possibly indicating preferred paths and patches during the draining process. Eventually, the following imbibition testified from a more homogeneous medium as compared to the drainage.

We reported a peculiar observation during the drainage phase: for a saturation value S^* close to $S_w \simeq 0.5$, the function $E/\ddot{u}$ experienced a sign change, also predicted by our calculations. Searching for the origin of that event, we concluded that it arises from a purely mechanical cause rather than from an electrokinetic phenomenon. At this critical saturation degree S^*, we showed that the P-wave modulus H is equally supported by the frame and the fluid phase, implying that frame displacement equals fluid displacement as the seismic wave goes through, causing the seismic attenuation of the "Biot" type and the coseismic seimoelectric field to vanish in the absence of filtration. This effect long known as "Biot's dynamic compatibility" has often been considered as an hypothetical object of study: the present saturation-dependent analysis in partially saturated sand constitutes a very original observation of this phenomenon. Further computations predicted that for a given material, critical saturation S^* would change according to imbibition and drainage phases, hence participating to the observed hysteresis in link with its connection to fluid homogeneity issues.

Considering that the shift in the polarity of $E/\ddot{u}$ coincides with a non-attenuated seismic wave, we expect the monitoring of both the seismoelectric field and the seismic attenuation to be capable of detecting critical saturation S^*. Interestingly, the coseismic seismoelectric signal may provide better access to fluid distribution than seismic attenuation does, and that for two reasons. First, the seismoelectric analysis requires simple time-picking to monitor the polarity of first arrivals, while attenuation calculation needs further assumptions on propagation geometry and geometrical spreading. Second, the change in coseismic seismoelectric signals is more marked (sign change) than that observed in seismic attenuation data (gradual decrease and increase with no sign change), hence facilitating its observability.

Finally, this study shows that propagating coseismic seismoelectric fields may be accurately measured by potential differences and might be strongly influenced by fluid heterogeneity. On this last topic, experimental apparatus comparable to our sandbox experiment could be more systematically used to gain further datasets with broader scope, as to investigate the effect of different heterogeneities types. The achievement of a joint spectral analysis on both seismic and seismoelectric fields would constitute a strong improvement towards the dynamic interpretation of seismoelectric measurements. However, further experimental studies demand additional theoretical and numerical developments, including a better understanding of the role patchy saturation may play in seismoelectric couplings (Müller et al. 2010; Rubino & Holliger 2012; Dupuy & Stovas 2013; Jougnot et al. 2013).

7 ACKNOWLEDGMENTS

JH thanks the French Ministry of Higher Education and Research for providing a PhD funding (2011-2014). The authors thank Total for providing an additional grant during the PhD thesis. This study has also benefited from the ANR programme of the French Government, especially via the TRANSEK project. The authors thank S. Garambois (ISTerre, France), J. Cresson (LMAP, Pau), V. Poydenot and P. Sénéchal (LFC-R, Pau) for their constructive discussions.

REFERENCES

Ageeva, O., Svetov, B., Sherman, G., & Shipulin, S., 1999. E-effect in rocks (data from laboratory experiments), *Russian Geology and Geophysics c/c of Geologiia i Geofizika*, **40**(8), 1232–1237.

Allègre, V., Lehmann, F., Ackerer, P., Jouniaux, L., & Sailhac, P., 2012. A 1-D modelling of streaming potential dependence on water content during drainage experiment in sand, *Geophysical Journal International*, **189**(1), 285–295.

Barrière, J., 2011. *Atténuation et dispersion des ondes P en milieu partiellement saturé : approche expérimentale*, Ph.D. thesis, Université de Pau et des Pays de l'Adour, France.

Barrière, J., Bordes, C., Brito, D., Sénéchal, P., & Perroud, H., 2012. Laboratory monitoring of P waves in partially saturated sand, *Geophysical Journal International*, **191**(3), 1152–1170.

Beamish, D., 1999. Characteristics of near-surface electrokinetic coupling, *Geophysical Journal International*, **137**(1), 231–242.

Biot, M., 1956a. Theory of propagation of elastic waves in a fluid-saturated porous solid. i. low-frequency range, *Journal of Acoustical Society of America*, **28**(2), 168–178.

Biot, M., 1956b. Theory of propagation of elastic waves in a fluid-saturated porous solid. ii. higher frequency range, *Journal of Acoustical Society of America*, **28**(2), 179–191.

Biot, M., 1962. Generalized theory of acoustic propagation in porous dissipative media, *Journal of Acoustical Society of America*, **34**(9), 1254–1264.

Blau, L. & Statham, L., 1936. Method and apparatus for seismic.

Block, G. & Harris, J., 2006. Conductivity dependence of seismoelectric wave phenomena in fluid-saturated sediments, *Journal of Geophysical Research*, **111**, B01304.

Bordes, C., 2005. *Etude expérimentale des phénomènes transitoires sismo-électromagnétiques: Mise en oeuvre au Laboratoire Souterrain de Rustrel, Pays d'Apt*, Ph.D. thesis, Université de Grenoble 1, France.

Bordes, C., Jouniaux, L., Dietrich, M., Pozzi, J., & Garambois, S., 2006. First laboratory measurements of seismo-magnetic conversions in fluid-filled Fontainebleau sand, *Geophysical Research Letters*, **33**, L01302.

Bordes, C., Jouniaux, L., Garambois, S., Dietrich, M., Pozzi, J., & Gaffet, S., 2008. Evidence of the theoretically predicted seismo-magnetic conversion, *Geophysical Journal International*, **174**(2), 489–504.

Bordes, C., Sénéchal, P., Barrière, J., Brito, D., Normandin, E., & Jougnot, D., 2015. Impact of water saturation on seismoelectric transfer functions: a laboratory study of coseismic phenomenon, *Geophysical Journal International*, **200**(3), 1317–1335.

Brie, A., Pampuri, F., Marsala, A., & Meazza, O., 1995. Shear sonic interpretation in gas-bearing sands, in SPE Annual Technical Conference, vol. 30595, pp. 701–710.

Burridge, R. & Vargas, C., 1979. The fundamental solution in dynamic poroelasticity, *Geophysical Journal International*, **58**(1), 61–90.

Cadoret, T., Marion, D., & Zinszner, B., 1995. Influence of frequency and fluid distribution on elastic wave velocities in partially saturated limestones, *Journal of Geophysical Research: Solid Earth (1978–2012)*, **100**(B6), 9789–9803.

Carcione, J., Picotti, S., Gei, D., & Rossi, G., 2006. Physics and seismic modeling for monitoring CO_2 storage, *Pure and Applied Geophysics*, **163**(1), 175–207.

De Ridder, S., Slob, E., & Wapenaar, K., 2009. Interferometric seismoelectric Green's function representations, *Geophysical Journal International*, **178**(3), 1289–1304.

Doussan, C. & Ruy, S., 2009. Prediction of unsaturated soil hydraulic conductivity with electrical conductivity, *Water Resources Research*, **45**(10).

Dupuis, J., Butler, K., & Kepic, A., 2007. Seismoelectric imaging of the vadose zone of a sand aquifer, *Geophysics*, **72**(6), A81.

Dupuy, B. & Stovas, A., 2013. Influence of frequency and saturation on avo attributes for patchy saturated rocks, *Geophysics*, **79**(1), B19–B36.

Dvorkin, J., Moos, D., Packwood, J., & Nur, A., 1999. Identifying patchy saturation from well logs, *Geophysics*, **64**(6), 1756–1759.

Frenkel, J., 1944. Orientation and rupture of linear macromolecules in dilute solutions under the influence of viscous flow, *Acta Physicochimica URSS*, **19**(1), 51–76.

Gallipoli, D., Gens, A., Sharma, R., & Vaunat, J., 2003. An elasto-plastic model for unsaturated soil incorporating the effects of suction and degree of saturation on mechanical behaviour., *Géotechnique.*, **53**(1), 123–136.

Gao, Y. & Hu, H., 2010. Seismoelectromagnetic waves radiated by a double couple source in a saturated porous medium, *Geophysical Journal International*, **181**(2), 873–896.

Garambois, S. & Dietrich, M., 2001. Seismoelectric wave conversions in porous media: Field measurements and transfer function analysis, *Geophysics*, **66**(5), 1417–1430.

Grobbe, N. & Slob, E., 2016. Seismo-electromagnetic thin-bed responses: Natural signal enhancements?, *Journal of Geophysical Research: Solid Earth*, **121**(4), 2460–2479.

Guichet, X., Jouniaux, L., & Pozzi, J., 2003. Streaming potential of a sand column in partial saturation conditions, *Journal of Geophysical Research*, **108**(B3).

Haartsen, M. & Pride, S., 1997. Electroseismic waves from point sources in layered media, *Journal of Geophysical Research*, **102**(B11), 24745–24769.

Haines, S., Pride, S., Klemperer, S., & Biondi, B., 2007. Seismoelectric imaging of shallow targets, *Geophysics*, **72**(2), G9.

Holzhauer, J., 2015. *Seismic and seismoelectric monitoring of an unconsolidated porous medium*, Ph.D. thesis, Université de Pau et des Pays de l'Adour, France.

Hu, H., Liu, J., & Wang, K., 2002. Attenuation and seismoelectric characteristics of dynamically compatible porous media, in 2002 SEG Annual Meeting, Expanded Abstracts, Society of Exploration Geophysicists.

Ivanov, A., 1939. Effect of electrization of earth layers by elastic waves passing through them, *Comptes Rendus (Doklady) de l'Academie des Sciences de L'URRS*, **24**, 42–45.

Ivanov, A., 1940. The seismoelectric effect of the second kind, in Proc Academy of Sciences USSR series of geography and geophysics, vol. 4, pp. 699–726.

Jackson, M., 2008. Characterization of multiphase electrokinetic coupling using a bundle of capillary tubes model, *Journal of Geophysical Research: Solid Earth*, **113**(B4).

Jackson, M., 2010. Multiphase electrokinetic coupling: Insights into the impact of fluid and charge distribution at the pore scale from a bundle of capillary tubes model, *Journal of Geophysical Research: Solid Earth*, **115**(B7).

Jougnot, D., Rubino, J., Carbajal, M., Linde, N., & Holliger, K., 2013. Seismoelectric effects due to mesoscopic heterogeneities, *Geophysical Research Letters*, **40**(10), 2033–2037.

Jouniaux, L. & Zyserman, F., 2016. A review on electrokinetically induced seismo-electrics, electro-seismics, and seismo-magnetics for earth sciences, *Solid Earth*, **7**(1), 249.

Knight, R. & Nolen-Hoeksema, R., 1990. A laboratory study of the dependence of elastic wave velocities on pore scale fluid distribution, *Geophysical Research Letters*, **17**(10), 1529–1532.

Linde, N., Jougnot, D., Revil, A., Matthäi, S., Arora, T., Renard, D., & Doussan, C., 2007. Streaming current generation in two-phase flow conditions, *Geophysical Research Letters*, **34**(3).

Mavko, G., Mukerji, T., & Dvorkin, J., 2003. *The rock physics handbook: Tools for seismic analysis of porous media*, Cambridge University Press.

Mesgouez, A., Lefeuve-Mesgouez, G., & Chambarel, A., 2005. Transient mechanical wave propagation in semi-infinite porous media using a finite element approach, *Soil Dynamics and Earthquake Engineering*, **25**(6), 421–430.

Monachesi, L., Rubino, J., Rosas-Carbajal, M., Jougnot, D., Linde, N., Quintal, B., & Holliger, K., 2015. An analytical study of seismoelectric signals produced by 1-D mesoscopic heterogeneities, *Geophysical Journal International*, **201**(1), 329–342.

Müller, T., Gurevich, B., & Lebedev, M., 2010. Seismic wave attenuation and dispersion resulting from wave-induced flow in porous rocks - A review, *Geophysics*, **75**(5), 75A147–75A164.

Nazarova-Cherrière, M., 2014. *Wettability study through X-ray micro-CT pore space imaging in EOR applied to LSB recovery process*, Ph.D. thesis, Université de Pau et des Pays de l'Adour, France.

Neev, J. & Yeatts, F., 1989. Electrokinetic effects in fluid-saturated poroelastic media, *Physical Review B*, **40**(13), 9135.

Parkhomenko, E., 1971. *Electrification phenomena in rocks*, Pleunum Press.

Parkhomenko, E. & Gaskarov, I., 1971. Borehole and laboratory studies of the seismoelectric effect of the second kind in rocks, *Izv. Akad. Sci. USSR, Physics Solid Earth*, **9**, 663–666.

Parkhomenko, I., Tsze-San, C., & Chien-San, C., 1964. A study of the influence of moisture on the magnitude of the seismoelectric effect in sedimentary rocks by a laboratory method, *Bull.(Izv.) Acad. Sci., USSR, Geophys. Ser*, **2**, 115–118.

Phillips, S., Ozbek, H., & Otto, R., 1978. Basic energy properties of electrolytic solutions database, in 6th Int. CODATA Conference.

Pride, S., 1994. Governing equations for the coupled electromagnetics and acoustics of porous media, *Physical Review B*, **50**(21), 15678–15696.

Pride, S., 2005. Relationships between seismic and hydrological properties, in Hydrogeophysics, pp. 253–290, Springer.

Pride, S. & Haartsen, M., 1996. Electroseismic wave properties, *Journal of the Acoustical Society of America*, **100**(3), 1301–1315.

Pride, S. & Morgan, F., 1991. Electrokinetic dissipation induced by seismic waves, *Geophysics*, **56**(7), 914–925.

Revil, A. & Jardani, A., 2010. Seismoelectric response of heavy oil reservoirs: theory and numerical modelling, *Geophysical Journal International*, **180**(2), 781–797.

Revil, A. & Mahardika, H., 2013. Coupled hydromechanical and electromagnetic disturbances in unsaturated porous materials, *Water resources research*, **49**(2), 744–766.

Revil, A., Linde, N., Cerepi, A., Jougnot, D., Matthäi, S., & Finsterle, S., 2007. Electrokinetic coupling in unsaturated porous media, *Journal of Colloid and Interface Science*, **313**(1), 315–327.

Revil, A., Barnier, G., Karaoulis, M., Sava, P., Jardani, A., & Kulessa, B., 2013. Seismoelectric coupling in unsaturated porous media: theory, petrophysics, and saturation front localization using an electroacoustic approach, *Geophysical Journal International*, **196**(2), 867–884.

Revil, A., Jardani, A., Sava, P., & Haas, A., 2015. *The Seismoelectric Method: Theory and Application*, John Wiley & Sons.

Rubino, J. & Holliger, K., 2012. Seismic attenuation and velocity dispersion in heterogeneous partially saturated porous rocks, *Geophysical Journal International*, **188**(3), 1088–1102.

Schoemaker, F., Grobbe, N., Schakel, M., De Ridder, S., Slob, E., & Smeulders, D., 2012. Experimental validation of the electrokinetic theory and development of seismoelectric interferometry by cross-correlation, *International Journal of Geophysics*, **2012**.

Simon, B., Zienkiewicz, O., & Paul, D., 1984. An analytical solution for the transient response of saturated porous elastic solids, *International Journal for Numerical and Analytical Methods in Geomechanics*, **8**(4), 381–398.

Slob, E. & Wapenaar, K., 2007. Electromagnetic Green's functions retrieval by cross-correlation and cross-convolution in media with losses, *Geophysical Research Letters*, **34**(5).

Strahser, M., Rabbel, W., & Schildknecht, F., 2007. Polarisation and slowness of seismoelectric signals: a case study, *Near Surface Geophysics*, **5**(2), 97–114.

Strahser, M., Jouniaux, L., Sailhac, P., Matthey, P., & Zillmer, M., 2011. Dependence of seismoelectric amplitudes on water content, *Geophysical Journal International*.

Teja, A. & Rice, P., 1981. Generalized corresponding states method for the viscosities of liquid mixtures, *Industrial & Engineering Chemistry Fundamentals*, **20**(1), 77–81.

Thompson, A. & Gist, G., 1993. Geophysical applications of electrokinetic conversion, *The Leading Edge*, **12**, 1169.

Thompson, R., 1936. The seismic electric effect, *Geophysics*, **1**(3), 327.

Voigt, W., 1928. Textbook of crystal physics, *BB Teubner, Leipzig*.

Walton, K., 1987. The effective elastic moduli of a random packing of spheres, *Journal of the Mechanics and Physics of Solids*, **35**(2), 213–226.

Wapenaar, K. & Fokkema, J., 2006. Green's function representations for seismic interferometry, *Geophysics*, **71**(4), SI33–SI46.

Wapenaar, K., Slob, E., & Snieder, R., 2006. Unified Green's function retrieval by cross correlation, *Physical Review Letters*, **97**(23), 234301.

Wapenaar, K., Slob, E., & Snieder, R., 2008. Seismic and electromagnetic controlled-source interferometry in dissipative media, *Geophysical Prospecting*, **56**(3), 419–434.

Warden, S., Garambois, S., Jouniaux, L., Brito, D., Sailhac, P., & Bordes, C., 2013. Seismoelectric wave propagation numerical modelling in partially saturated materials, *Geophysical Journal International*, **194**(3), 1498–1513.

Wei, C. & Muraleetharan, K., 2002a. A continuum theory of porous media saturated by multiple immiscible fluids: I. linear poroelasticity, *International Journal of Engineering Science*, **40**(16), 1807–1833.

Wei, C. & Muraleetharan, K., 2002b. A continuum theory of porous media saturated by multiple immiscible fluids: Ii. lagrangian description and variational structure, *International Journal of Engineering Science*, **40**(16), 1835–1854.

Wood, A., 1955. *A textbook of sound*, G. Bell and sons.

Zhu, Z. & Toksöz, M., 2003. Effects of saturant conductivity on seismoelectric conversion, Tech. rep., Massachusetts Institute of Technology. Earth Resources Laboratory.

Zhu, Z. & Toksöz, M., 2005. Seismoelectric and seismomagnetic measurements in fractured borehole models, *Geophysics*, **70**, F45.

Zhu, Z. & Toksöz, M., 2013. Experimental measurements of the streaming potential and seismoelectric conversion in Berea sandstone, *Geophysical Prospecting*, **61**(3), 688–700.

Zhu, Z., Haartsen, M., & Toksöz, M., 1999. Experimental studies of electrokinetic conversions in fluid-saturated borehole models, *Geophysics*, **64**(5), 1349.

Zhu, Z., Haartsen, M., & Toksöz, M., 2000. Experimental studies of seismoelectric conversions in fluid-saturated porous media, *Journal of Geophysical Research*, **105**(B12), 28055–28.

LIST OF FIGURES

1 Pictures of the experimental set-up. a) Global view of the sandbox with pneumatic source (hold by the red frame). b) Detail of the pneumatic source. The piston on the right hand side is moved forward towards the hitting plate, where a transducer, in the upper left, records the acceleration. c) Partial emptying of the sandbox after a measuring campaign: half of the measuring plane is covered in a 25 cm thick sand-layer while the other half is visible. In particular, one sees the vertical electrodes measuring the electric field in the same horizontal plane where the accelerometers, also visible though buried in the sand, measure the seismic field while the other half is covered by a 25 cm thick sand-layer

2 Schematic view of the sandbox from above. The hitting-plate of the pneumatic source is pictured in dark gray at the right side of the sandbox. The electrode array, in line with the hitting plate, is shown as a series of 30 aligned blue circles, saving the yellow colour for the common reference electrode. The electric potential at position i is measured with respect to the common reference as $V_i - V_{ref}$. The 20 accelerometers disposed on two parallel lines are visible as small red rectangles. $\ddot{u}_i$ is the acceleration measurement at position i. A last accelerometer is placed on the punch for direct recording of the source acceleration. The experimental set-up also includes 4 injections wells pictured as large circles in the corners of the sandbox as well as 7 water sensors, from which 5 lay within the measuring plane sketched as blue rectangles and further 2 belong to the vertical plane (not seen here).

3 a) Acceleration measurements $\ddot{u}$ vs time recorded at the hitting plate during a series of shots by the home-made pneumatic source. The 25 superimposed shots were obtained for $S_w = 0.95$ and $\sigma_f = 2.5\ mS \cdot m^{-1}$. In red, the averaged signal in time filtered by a low pass Butterworth filter of degree 8 and cutoff frequency 25 kHz. b) In black, the corresponding 25 spectra associated to the signals shown in a). In red, the averaged spectrum subjected to the same filtering process as in a).

4 a) and b): Schematic representations of electric and seismic acquisition arrays in the experimental sandbox, for two geometries of dipole reconstruction at offset 5.8 cm. Each electrode rod is sketched as a blue circle. In a), electric potential differences ΔV are reconstructed from dipoles of varying dipole-length l_{dip}, all centered on $e_{5.8\ cm}$. These dipoles representing the mid-point geometry are labeled ΔV_M. In b), dipoles share $e_{5.8\ cm}$ as a common first electrode and are labeled ΔV_F; the last electrode in yellow is the common reference electrode. c) and d): Experimental dataset of potential differences ΔV_M and ΔV_F at offset 5.8 cm measured vs time, for varying dipole length l_{dip}. e) and f): Same experimental electric dataset as in c) and d) normalized in order to compare electric potentials ΔV_M and ΔV_F with respect to seismic acceleration $\ddot{u}$ recorded at the same offset 5.8 cm. Corresponding colours in thick lines traduce identical dipole lengths in electric data through a) to f).

5 a) and b): Maximum of electric potential difference ΔV as a function of l_{dip}/λ. a) presents mid-point potential ΔV_M at various offsets while b) shows first-point potential ΔV_F. c) and d): Electric field amplitudes deduced from potential differences shown in a) and b) using eq. (3), and giving respectively $|E_M|$ and $|E_F|$. e) and f): Representation of time $t_{max}(\Delta V)$, picked at maximum amplitude of the electric signal, divided by time $t_{max}(\ddot{u})$, picked at maximum amplitude of the seismic signal, as a function of l_{dip}/λ. Mid-point potentials ΔV_M are used in e) whereas first-point potential ΔV_F are used in f).

6 Electric field amplitudes $|E_M|$ calculated on mid-point dipoles of length $l_{dip} = 1.8\ cm$ vs electric field amplitudes values $|E_F|$ computed on first-electrode dipole of $l_{dip} = 0.9\ cm$ length, at corresponding offsets. These data come from a variety of experiments performed at various saturation rates S_w and various fluid conductivity σ_f: each symbol in the legend corresponds to a couple of parameters (S_w, σ_f) whereas the colour of the symbol gives the offset where the electric field has been measured. The dashed line represents the identity function.

7 Modulus of the transfer function $|E/\ddot{u}|$ as a function of frequency f computed from eq. (1), according to the medium parameters given in Table 1. The transfer function is computed for three various fluid conductivities at full saturation $S_w = 1$. The Biot frequency is shown as a red dotted line.

8 Acceleration $\ddot{u}$ (a to c) and electric field E_M, (d to f) data, averaged on about 50 shots, obtained at various offsets for experiments performed under different fluid conductivities σ_f, and represented vs time. Corresponding colours in thick lines traduce corresponding offsets in seismic and seismoelectric figures. Relative amplitudes are preserved as to give 50 $m \cdot s^{-2}$ per vertical division for the seismic field and 0.5 $V \cdot m^{-1}$ per division for the electric field. For the sake of data readability, electric curves were flipped in polarity.

9 Experimental and theoretical values $|E/\ddot{u}|$ represented vs fluid conductivity σ_f. Experimental values of $|E/\ddot{u}|$ are shown with coloured dots for various offsets at a given fluid conductivity σ_f. The averaged values and their standard deviation are represented as black crosses. Error bars on conductivity were estimated to be of the order $0.5\ mS{\cdot}m^{-1}$. The dashed and continuous lines correspond to the dynamic seismoelectric transfer function from eq. (1), respectively computed for $(S_w = 0.95,\ f = 0.5\ kHz)$ and $(S_w = 0.95,\ f = 2\ kHz)$, all further physical properties matching those. An additional data point displayed at a conductivity value of 11.7 $mS \cdot m^{-1}$ was obtained from averaging experimental values taken from Bordes et al. (2015).

10 P-wave velocities V_P deduced from time-picking of the first seismic arrival during time-lapse monitored experiments with varying saturation S_w. The measurements were performed during initial imbibition, subsequent drainage and following re-imbibition. Velocity time-picking was performed between offsets 10 to 23 cm. Error bars in velocity amplitudes were calculated from a linear regression of the time-picking vs offsets on a 80% confidence interval. The velocity models are represented by solid and dashed lines matching the colour of the corresponding experimental points. They were jointly obtained by least-square inversion on these V_P data and on the $E/\ddot{u}$ data from Fig. 12, while adapting the effective fluid modulus K_f. All the velocity models are computed at a frequency $f = 1.5\ kHz$.

11 Evolution of seismic (blue) and electric (red) signals vs time as a function of changes in water saturation S_w, for a set of experimental data acquired during drainage. Note that while water saturation is determined by the origin ordinate of each seismic curve, the vertical divisions on this same axis enable to get back to the signals amplitudes. The scale is of $10\ m \cdot s^{-2}$ per vertical division for the seismic field, and $0.025\ V \cdot m^{-1}$ per vertical division for the electric field. The origin on the time axis coincides with the initial punch of the pneumatic source. Seismic signals were taken for the first and second receivers at respective offsets a) $4.8\ cm$ and b) $5.8\ cm$; electric signals were was taken for the mid-point dipole of length $1.8\ cm$ placed at offset a) $3.9\ cm$ and b) $5.8\ cm$. Seismic signals in blue result from a stack 25. Electric signals in bold, dashed and light lines result respectively from stacks 50, 25 and 5.

12 Experimental values of local $E/\ddot{u}$ ratio estimated during time-lapse monitored experiments with varying saturation S_w. The measurements -performed during initial imbibition, subsequent drainage and following re-imbibition - are represented for a fluid conductivity of $7.2\ mS \cdot m^{-1}$. We considered electric data acquired at offset $3.9\ cm$, combined to seismic amplitudes extrapolated to a corresponding offset. Systematic error bars on the amplitude of $E/\ddot{u}$ are of the order of $1\ V \cdot s^2 \cdot m^{-2}$ based on the uncertainties in electric and seismic pickings. The horizontal error bars on saturation are computed from the difference between the minimum and maximum values of the recorded saturation by the capacitance probes. The estimates of the transfer function are represented by solid and dashed lines matching the colour of the corresponding experimental points. They were jointly obtained by least-square inversion on these $E/\ddot{u}$ ratios and on the associated V_P data from Fig. 10, while adapting the effective fluid modulus K_f. Models based on an effective fluid modulus of the Brie type with exponent e are noted $K_{B\ e}$, while K_R points at an effective fluid modulus based on the Reuss average. Since the dynamic transfer functions eq. (1) is complex, the theoretical functions in the present figure are drawn as sign(real$(E/\ddot{u})) \times \mid E/\ddot{u} \mid$. All model predictions are computed at a frequency $f = 1.5\ kHz$.

13 a) Inverse of the seismic quality factor $Q^{-1}\ vs\ S_w$, computed from eq. (1) using properties given in Table 1. Curves are obtained for four distinct estimations of the effective fluid modulus $K_f(S_w)$, as K_R and $K_{B\ e}$ with $e = [9, 32, 61]$. For each case a star, matching the curve in colour, gives the exact location of the critical saturation S^* for which attenuation vanishes. b) Ratio of the fluid over frame displacements $u_f/\ u\ vs$ saturation S_w. Filtration velocity w is positive when $u_f/u > 1$ and negative when $u_f/u < 1$. The displacements are computed for the same models as in a); note that corresponding critical saturations S^* coincide with $u_f/u = 1$ for which there is no filtration. c) $H(S_w)$, H_{fr} and $H_f(S_w)\ vs\ S_w$ computed for two distinct models of effective fluid modulus $K_{B\ 9}$ and $K_{B\ 61}$. Corresponding stars give the exact location of critical saturation S^*.

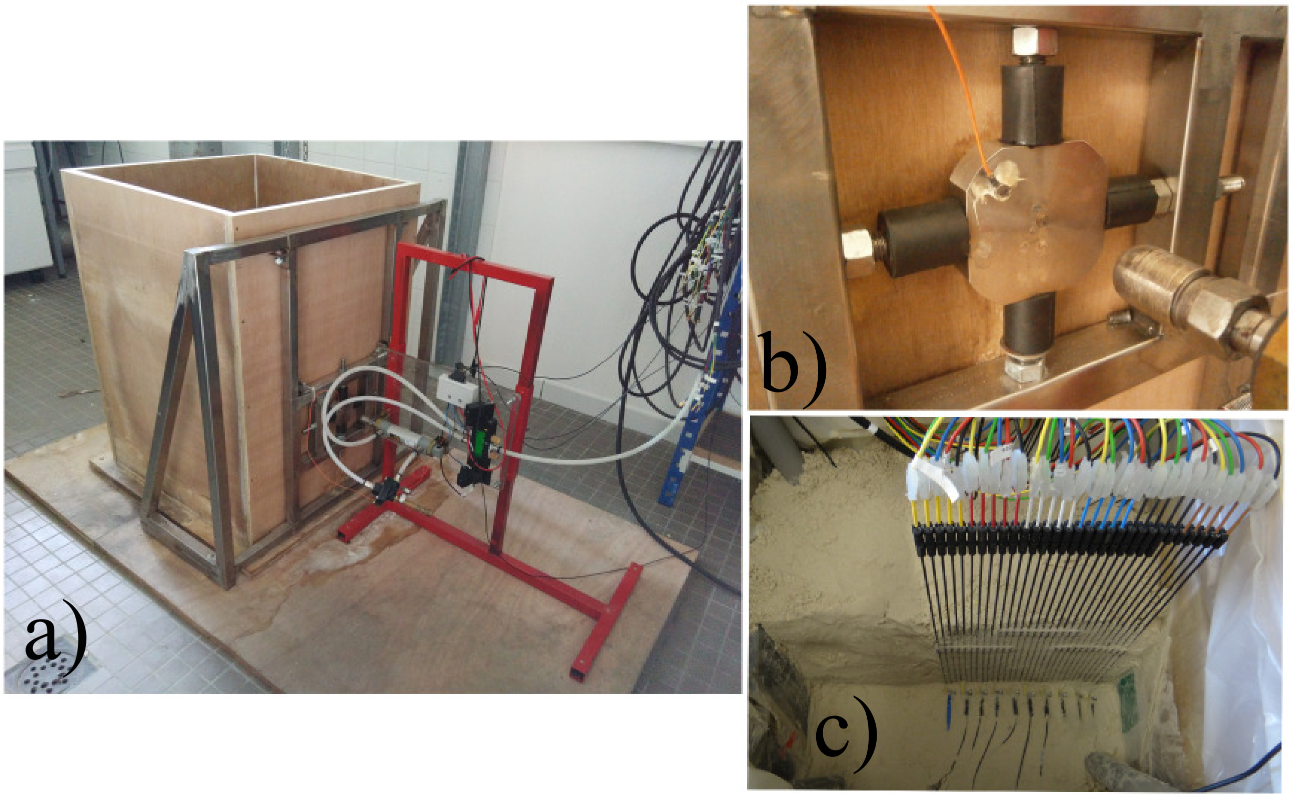

Figure 1. Pictures of the experimental set-up. a) Global view of the sandbox with pneumatic source (hold by the red frame). b) Detail of the pneumatic source. The piston on the right hand side is moved forward towards the hitting plate, where a transducer, in the upper left, records the acceleration. c) Partial emptying of the sandbox after a measuring campaign: half of the measuring plane is covered in a 25 cm thick sand-layer while the other half is visible. In particular, one sees the vertical electrodes measuring the electric field in the same horizontal plane where the accelerometers, also visible though buried in the sand, measure the seismic field while the other half is covered by a 25 cm thick sand-layer

.

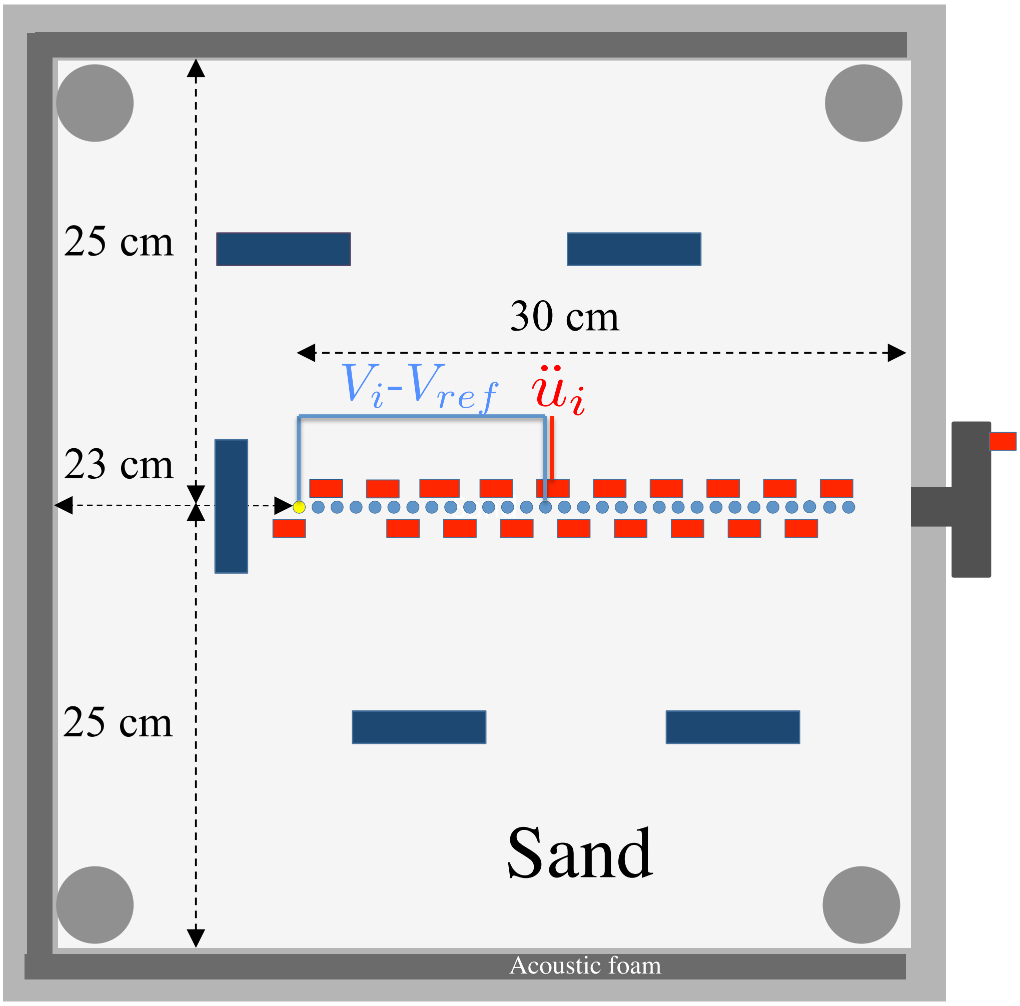

Figure 2. Schematic view of the sandbox from above. The hitting-plate of the pneumatic source is pictured in dark gray at the right side of the sandbox. The electrode array, in line with the hitting plate, is shown as a series of 30 aligned blue circles, saving the yellow colour for the common reference electrode. The electric potential at position i is measured with respect to the common reference as $V_i - V_{ref}$. The 20 accelerometers disposed on two parallel lines are visible as small red rectangles. $\ddot{u}_i$ is the acceleration measurement at position i. A last accelerometer is placed on the punch for direct recording of the source acceleration. The experimental set-up also includes 4 injections wells pictured as large circles in the corners of the sandbox as well as 7 water sensors, from which 5 lay within the measuring plane sketched as blue rectangles and further 2 belong to the vertical plane (not seen here).

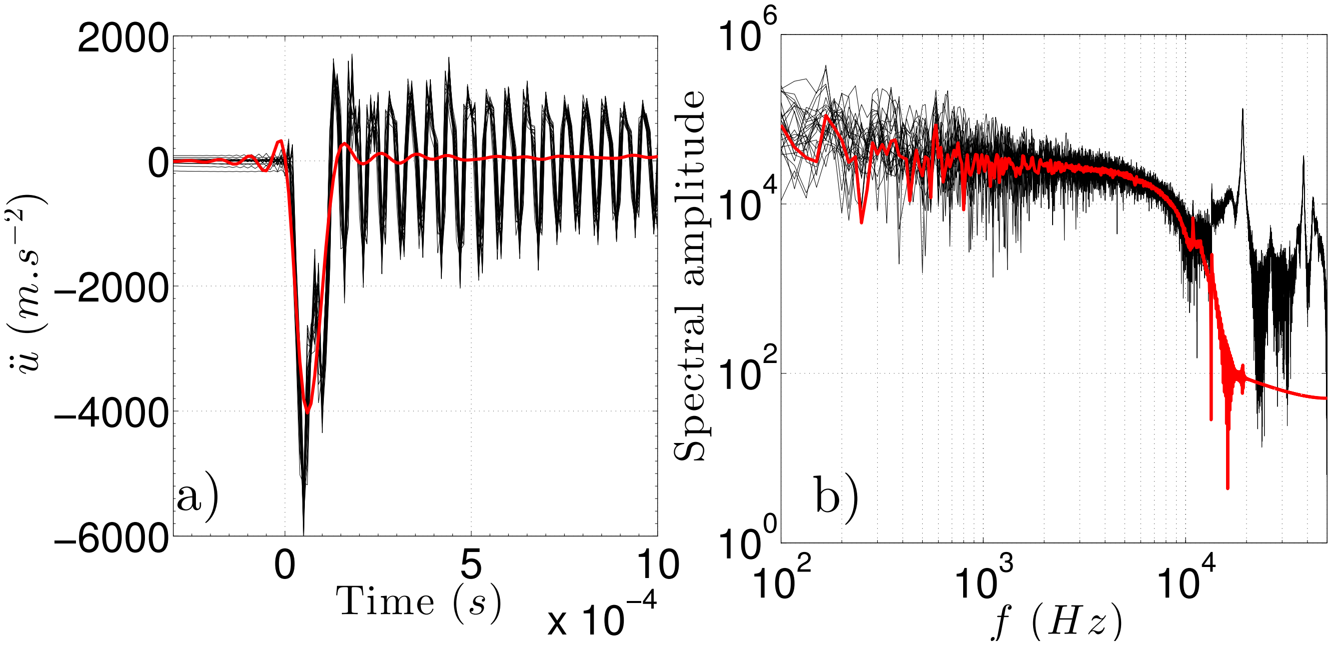

Figure 3. a) Acceleration measurements $\ddot{u}$ vs time recorded at the hitting plate during a series of shots by the home-made pneumatic source. The 25 superimposed shots were obtained for $S_w = 0.95$ and $\sigma_f = 2.5\ mS \cdot m^{-1}$. In red, the averaged signal in time filtered by a low pass Butterworth filter of degree 8 and cutoff frequency 25 kHz. b) In black, the corresponding 25 spectra associated to the signals shown in a). In red, the averaged spectrum subjected to the same filtering process as in a).

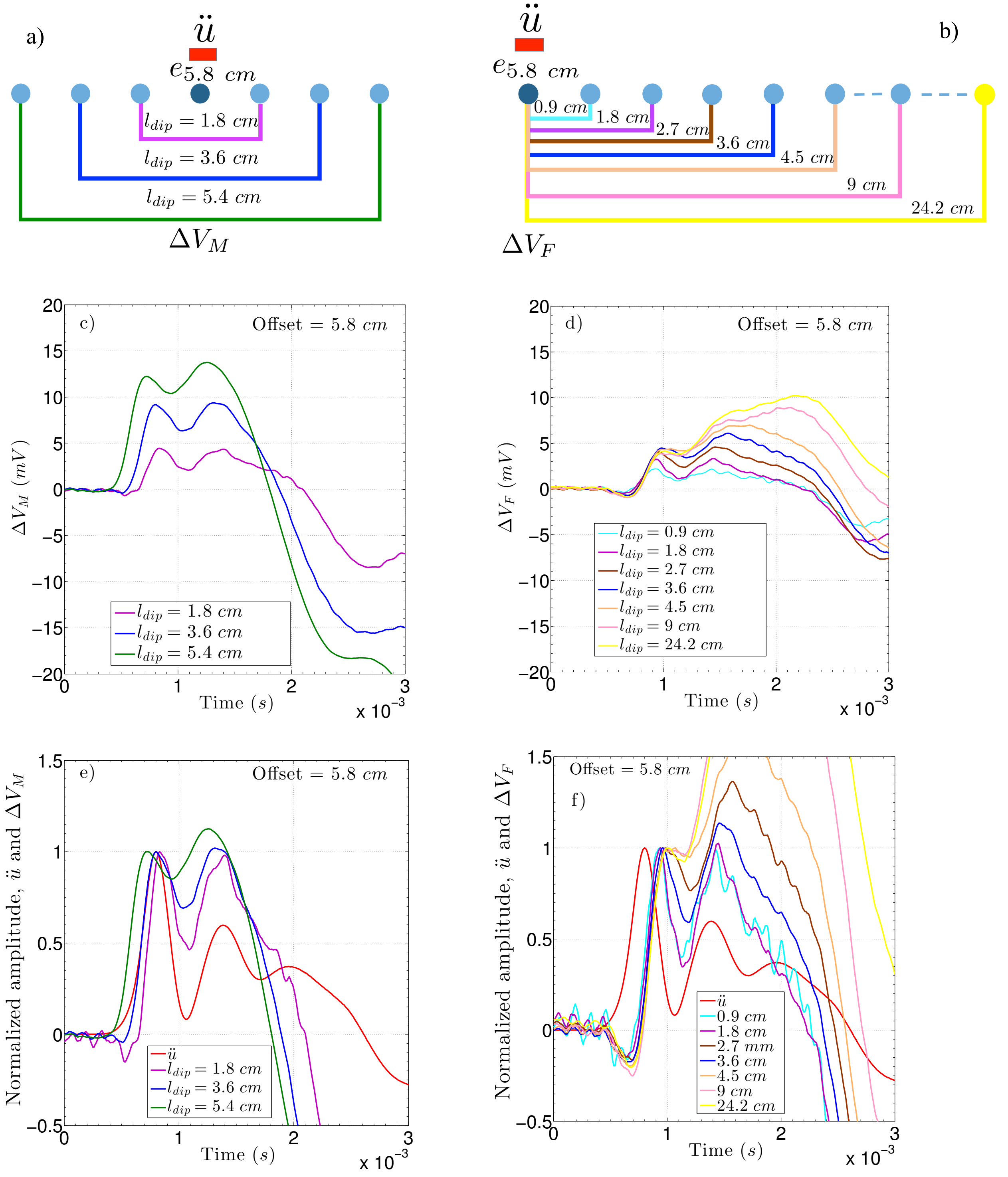

Figure 4. a) and b): Schematic representations of electric and seismic acquisition arrays in the experimental sandbox, for two geometries of dipole reconstruction at offset 5.8 cm. Each electrode rod is sketched as a blue circle. In a), electric potential differences ΔV are reconstructed from dipoles of varying dipole-length l_{dip}, all centered on $e_{5.8\ cm}$. These dipoles representing the mid-point geometry are labeled ΔV_M. In b), dipoles share $e_{5.8\ cm}$ as a common first electrode and are labeled ΔV_F; the last electrode in yellow is the common reference electrode. c) and d): Experimental dataset of potential differences ΔV_M and ΔV_F at offset 5.8 cm measured vs time, for varying dipole length l_{dip}. e) and f): Same experimental electric dataset as in c) and d) normalized in order to compare electric potentials ΔV_M and ΔV_F with respect to seismic acceleration $\ddot{u}$ recorded at the same offset 5.8 cm. Corresponding colours in thick lines traduce identical dipole lengths in electric data through a) to f).

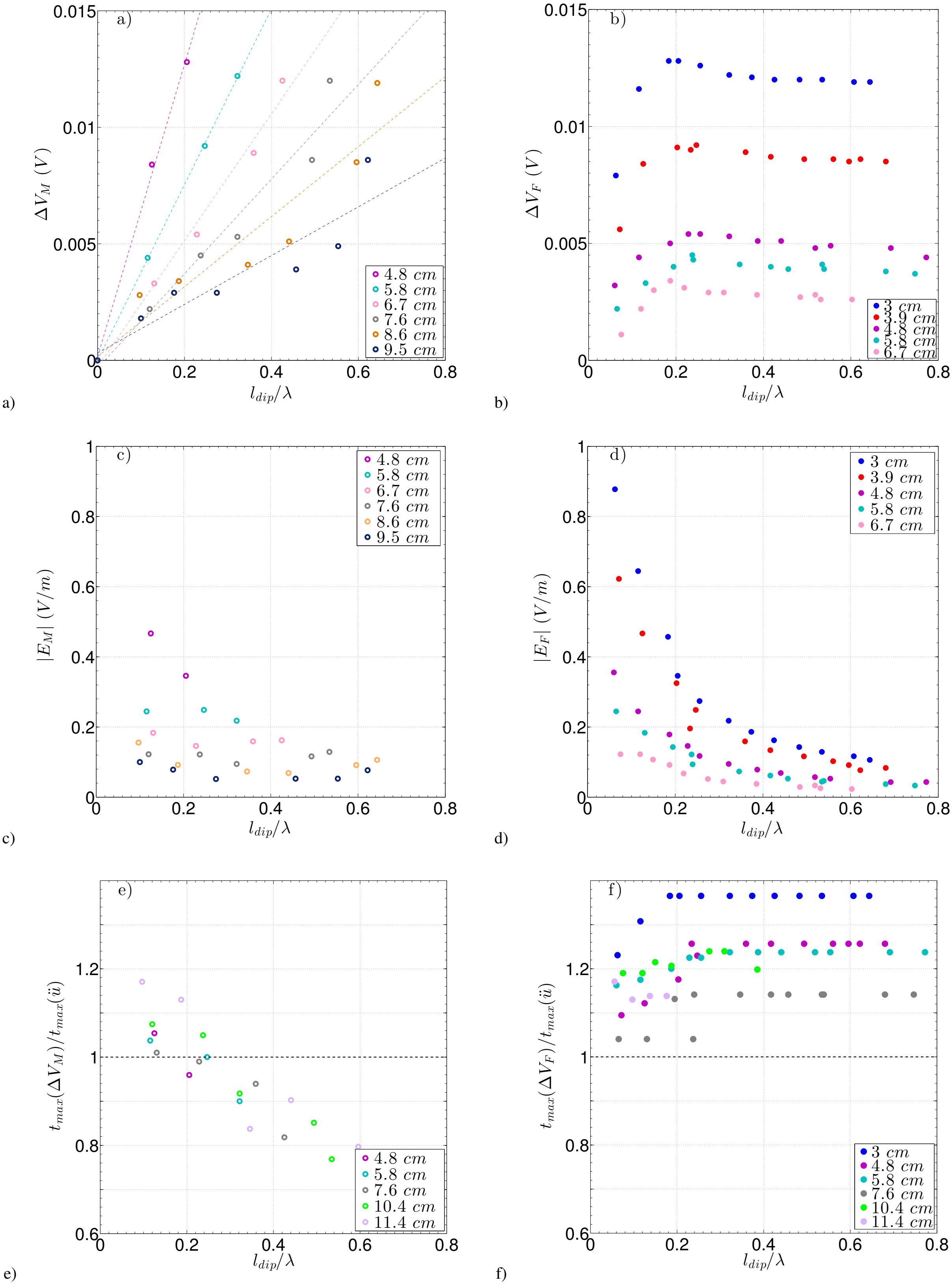

a)

b)

c)

d)

e)

f)

Figure 5. a) and b): Maximum of electric potential difference ΔV as a function of l_{dip}/λ. a) presents mid-point potential ΔV_M at various offsets while b) shows first-point potential ΔV_F. c) and d): Electric field amplitudes deduced from potential differences shown in a) and b) using eq. (3), and giving respectively $|E_M|$ and $|E_F|$. e) and f): Representation of time $t_{max}(\Delta V)$, picked at maximum amplitude of the electric signal, divided by time $t_{max}(\ddot{u})$, picked at maximum amplitude of the seismic signal, as a function of l_{dip}/λ. Mid-point potentials ΔV_M are used in e) whereas first-point potential ΔV_F are used in f).

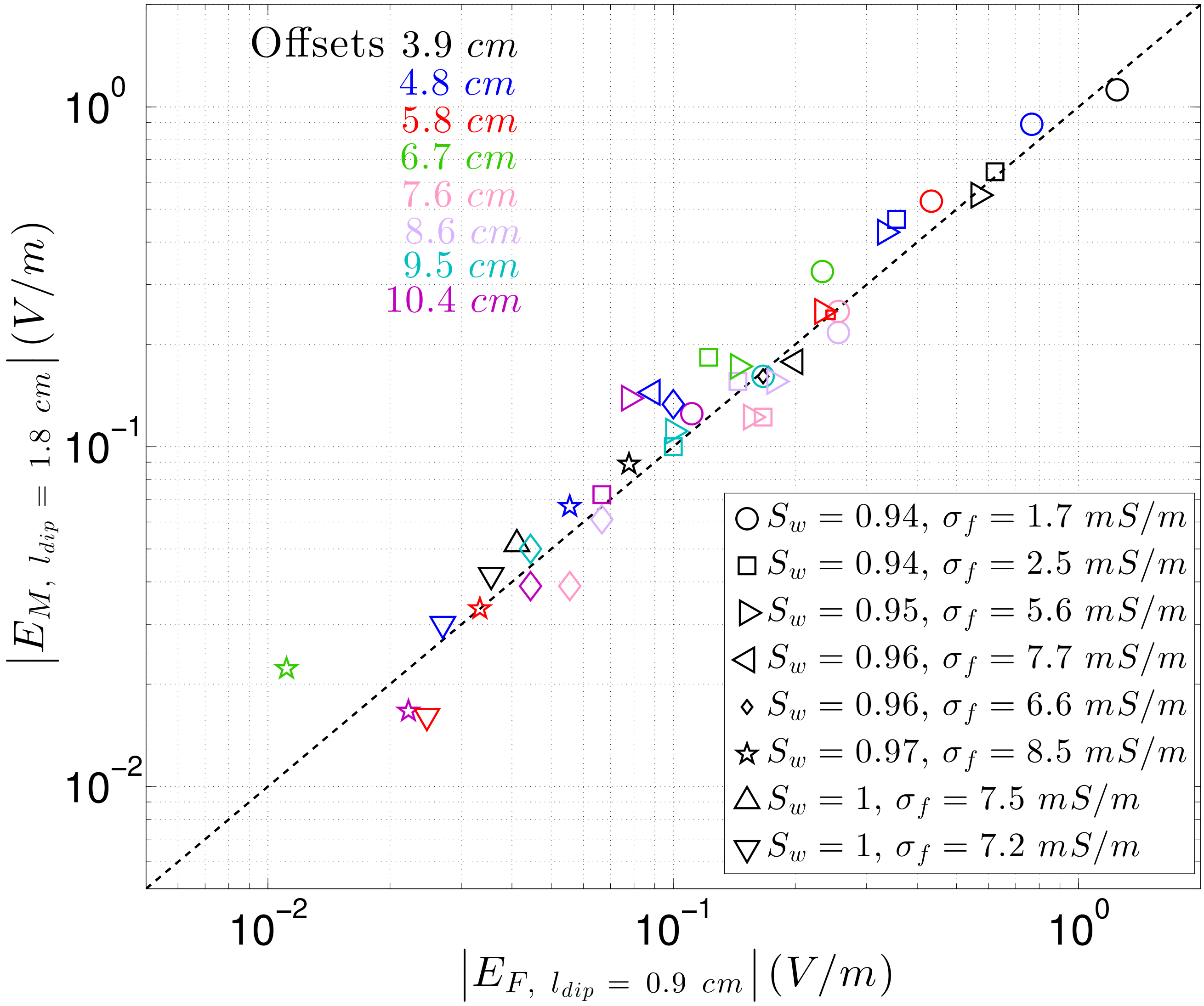

Figure 6. Electric field amplitudes $|E_M|$ calculated on mid-point dipoles of length $l_{dip} = 1.8\ cm$ vs electric field amplitudes values $|E_F|$ computed on first-electrode dipole of $l_{dip} = 0.9\ cm$ length, at corresponding offsets. These data come from a variety of experiments performed at various saturation rates S_w and various fluid conductivity σ_f: each symbol in the legend corresponds to a couple of parameters (S_w, σ_f) whereas the colour of the symbol gives the offset where the electric field has been measured. The dashed line represents the identity function.

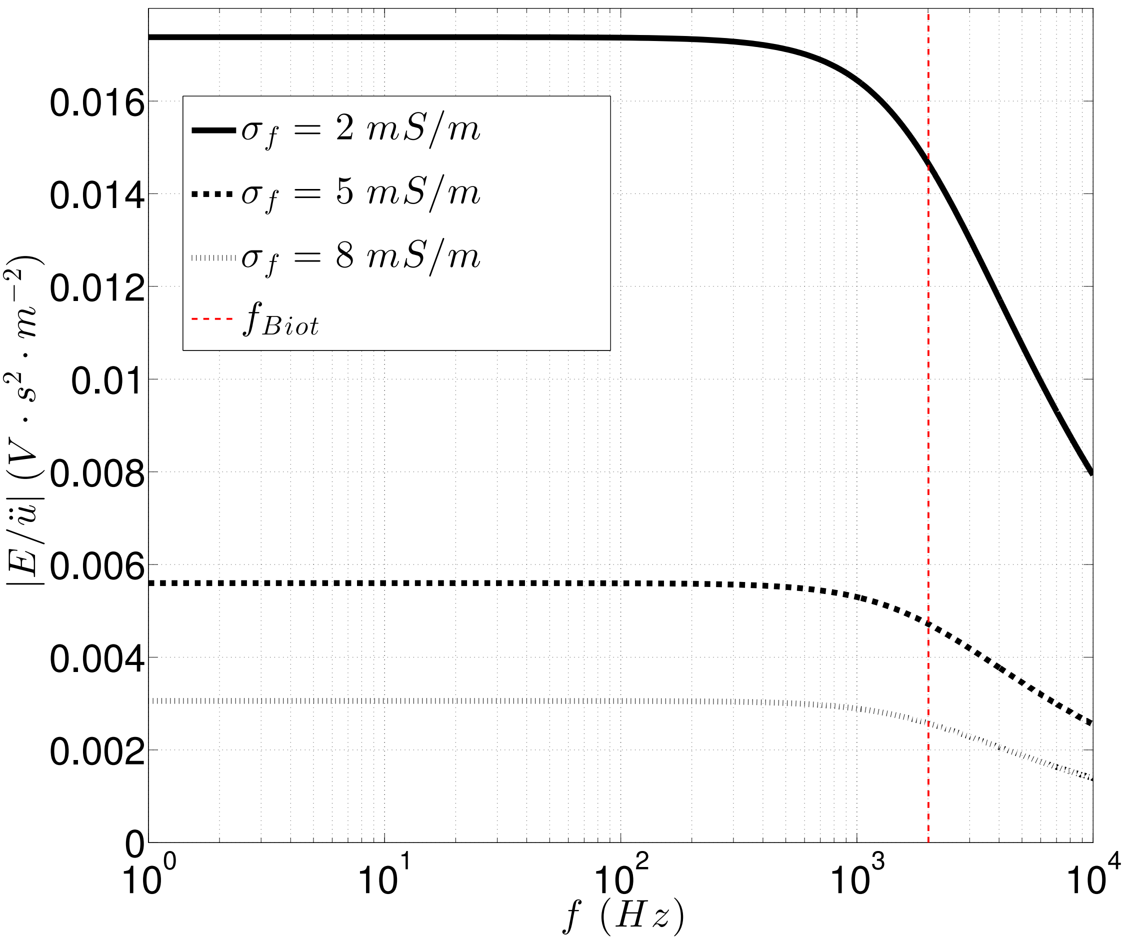

Figure 7. Modulus of the transfer function $|E/\ddot{u}|$ as a function of frequency f computed from eq. (1), according to the medium parameters given in Table 1. The transfer function is computed for three various fluid conductivities at full saturation $S_w = 1$. The Biot frequency is shown as a red dotted line.

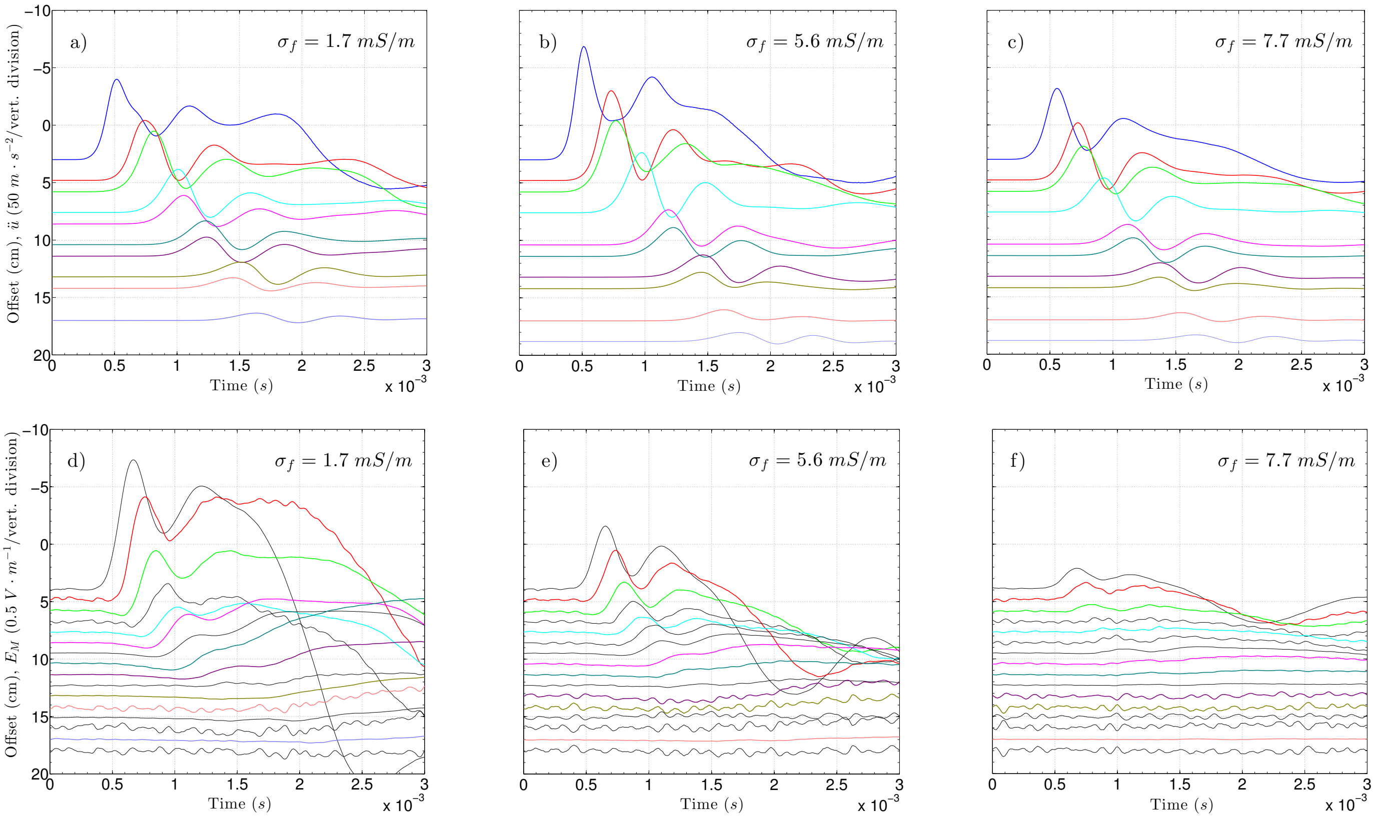

Figure 8. Acceleration $\ddot{u}$ (a to c) and electric field E_M, (d to f) data, averaged on about 50 shots, obtained at various offsets for experiments performed under different fluid conductivities σ_f, and represented vs time. Corresponding colours in thick lines traduce corresponding offsets in seismic and seismoelectric figures. Relative amplitudes are preserved as to give 50 $m \cdot s^{-2}$ per vertical division for the seismic field and 0.5 $V \cdot m^{-1}$ per division for the electric field. For the sake of data readability, electric curves were flipped in polarity.

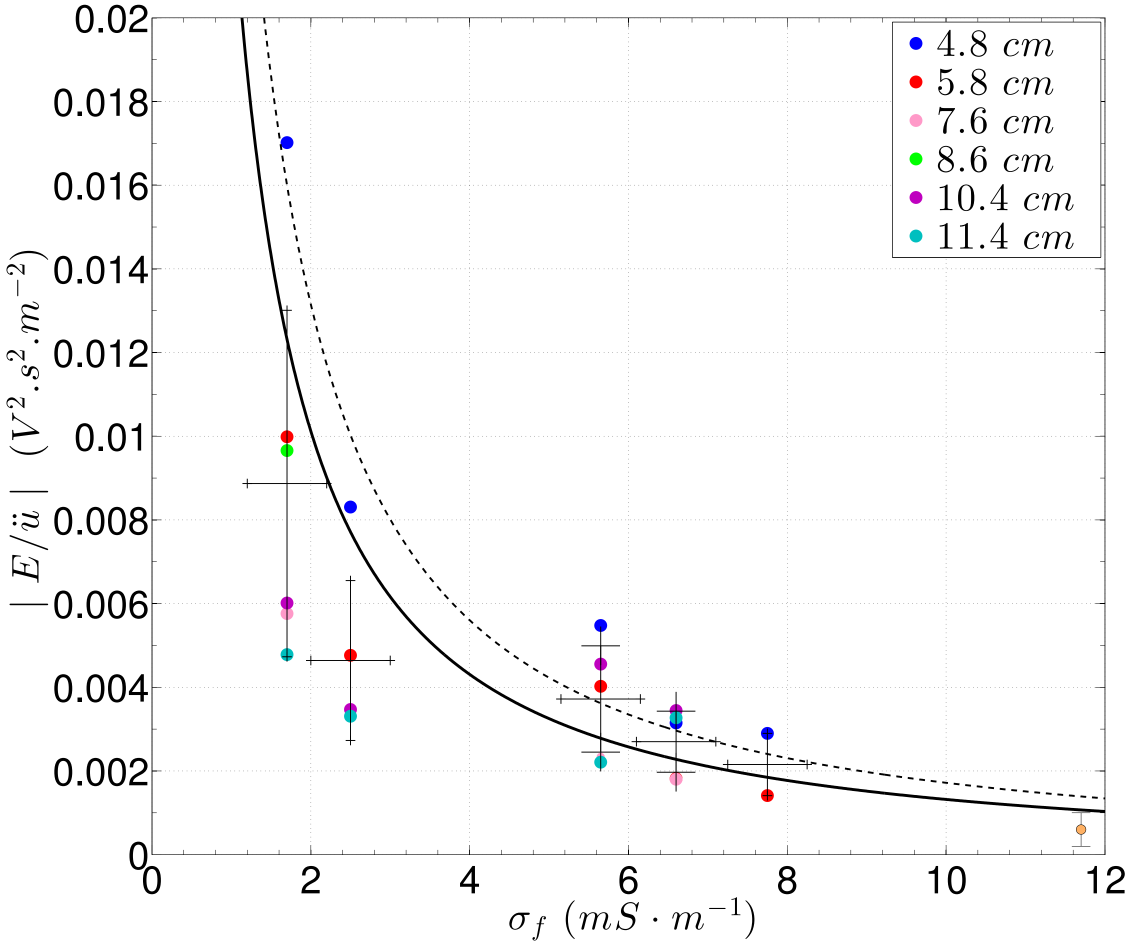

Figure 9. Experimental and theoretical values $|E/\ddot{u}|$ represented vs fluid conductivity σ_f. Experimental values of $|E/\ddot{u}|$ are shown with coloured dots for various offsets at a given fluid conductivity σ_f. The averaged values and their standard deviation are represented as black crosses. Error bars on conductivity were estimated to be of the order $0.5\ mS \cdot m^{-1}$. The dashed and continuous lines correspond to the dynamic seismoelectric transfer function from eq. (1), respectively computed for $(S_w = 0.95,\ f = 0.5\ kHz)$ and $(S_w = 0.95,\ f = 2\ kHz)$, all further physical properties matching those. An additional data point displayed at a conductivity value of $11.7\ mS \cdot m^{-1}$ was obtained from averaging experimental values taken from Bordes et al. (2015).

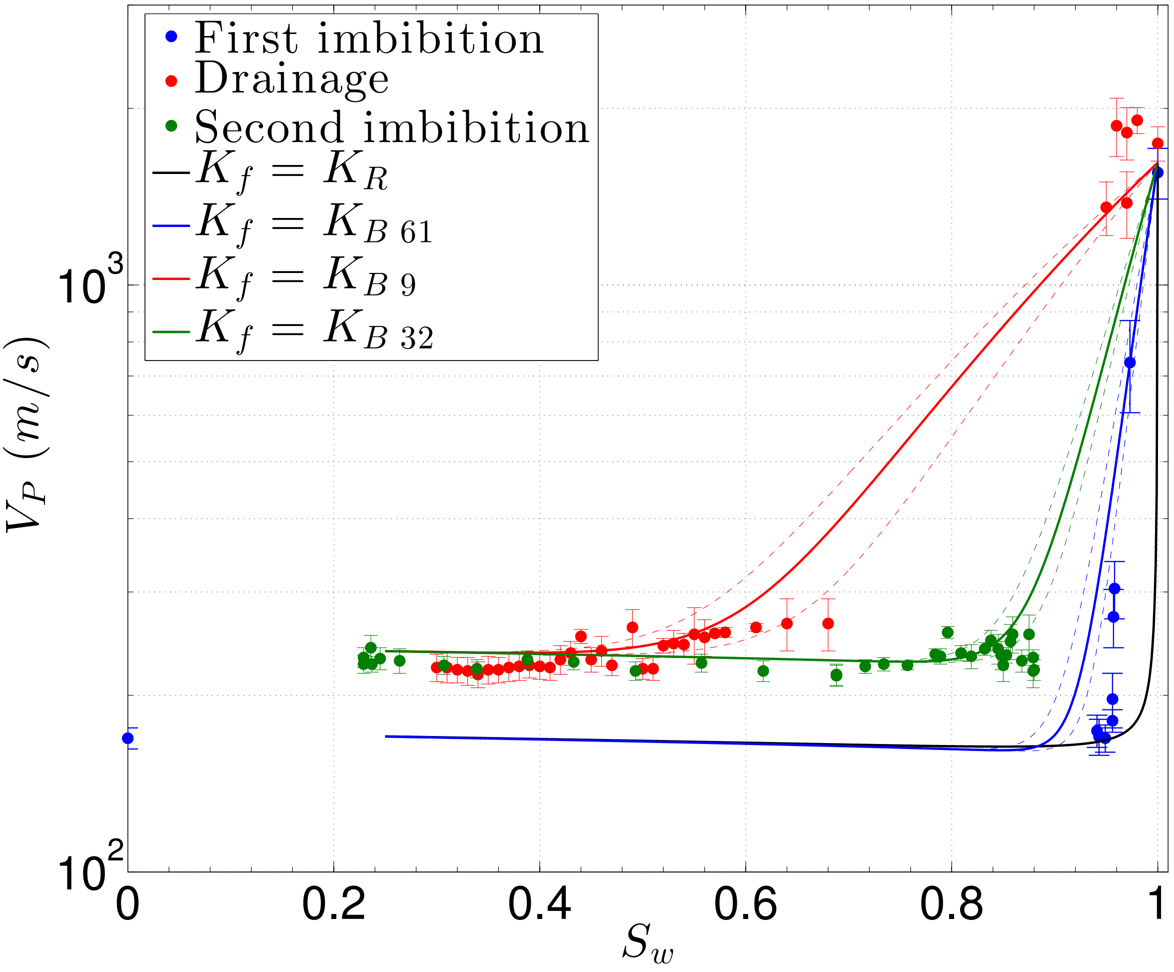

Figure 10. P-wave velocities V_P deduced from time-picking of the first seismic arrival during time-lapse monitored experiments with varying saturation S_w. The measurements were performed during initial imbibition, subsequent drainage and following re-imbibition. Velocity time-picking was performed between offsets 10 to 23 cm. Error bars in velocity amplitudes were calculated from a linear regression of the time-picking vs offsets on a 80% confidence interval. The velocity models are represented by solid and dashed lines matching the colour of the corresponding experimental points. They were jointly obtained by least-square inversion on these V_P data and on the $E/\ddot{u}$ data from Fig. 12, while adapting the effective fluid modulus K_f. All the velocity models are computed at a frequency $f = 1.5\,kHz$.

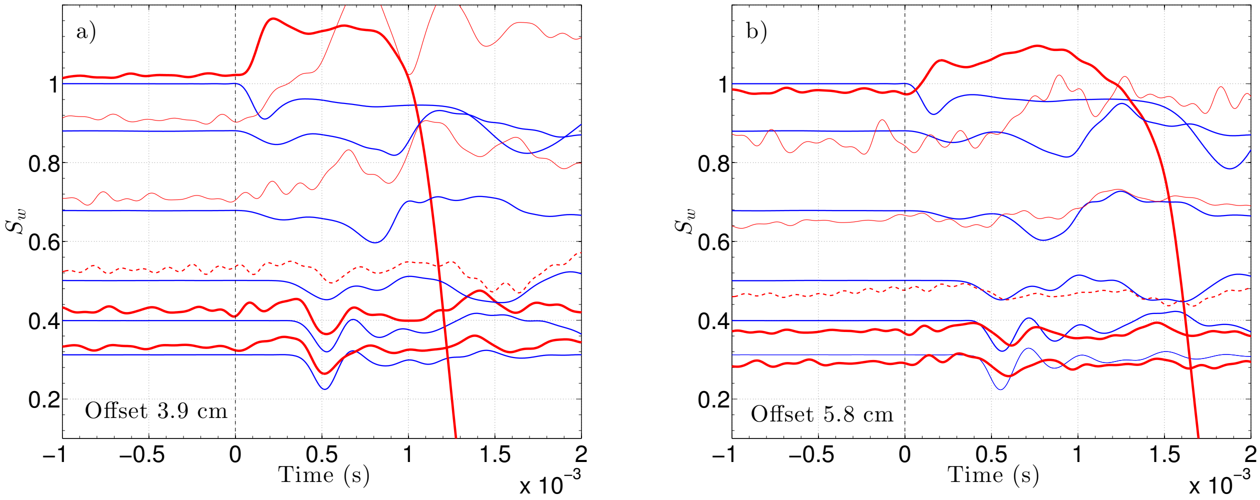

Figure 11. Evolution of seismic (blue) and electric (red) signals vs time as a function of changes in water saturation S_w, for a set of experimental data acquired during drainage. Note that while water saturation is determined by the origin ordinate of each seismic curve, the vertical divisions on this same axis enable to get back to the signals amplitudes. The scale is of $10\ m \cdot s^{-2}$ per vertical division for the seismic field, and $0.025\ V \cdot m^{-1}$ per vertical division for the electric field. The origin on the time axis coincides with the initial punch of the pneumatic source. Seismic signals were taken for the first and second receivers at respective offsets a) $4.8\ cm$ and b) $5.8\ cm$; electric signals were was taken for the mid-point dipole of length $1.8\ cm$ placed at offset a) $3.9\ cm$ and b) $5.8\ cm$. Seismic signals in blue result from a stack 25. Electric signals in bold, dashed and light lines result respectively from stacks 50, 25 and 5.

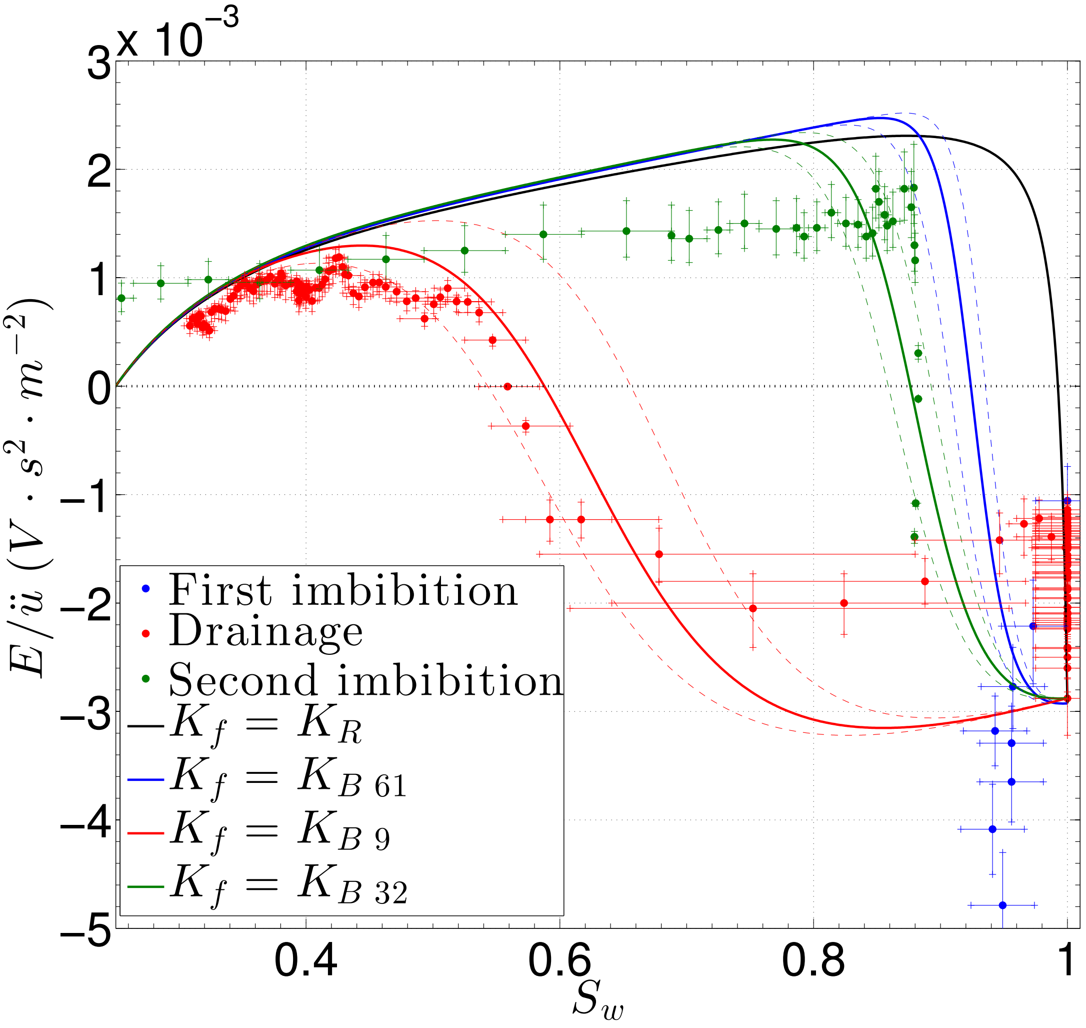

Figure 12. Experimental values of local $E/\ddot{u}$ ratio estimated during time-lapse monitored experiments with varying saturation S_w. The measurements - performed during initial imbibition, subsequent drainage and following re-imbibition - are represented for a fluid conductivity of $7.2\ mS \cdot m^{-1}$. We considered electric data acquired at offset $3.9\ cm$, combined to seismic amplitudes extrapolated to a corresponding offset. Systematic error bars on the amplitude of $E/\ddot{u}$ are of the order of $1\ V \cdot s^2 \cdot m^{-2}$ based on the uncertainties in electric and seismic pickings. The horizontal error bars on saturation are computed from the difference between the minimum and maximum values of the recorded saturation by the capacitance probes. The estimates of the transfer function are represented by solid and dashed lines matching the colour of the corresponding experimental points. They were jointly obtained by least-square inversion on these $E/\ddot{u}$ ratios and on the associated V_P data from Fig. 10, while adapting the effective fluid modulus K_f. Models based on an effective fluid modulus of the Brie type with exponent e are noted $K_{B\ e}$, while K_R points at an effective fluid modulus based on the Reuss average. Since the dynamic transfer functions eq. (1) is complex, the theoretical functions in the present figure are drawn as sign(real($E/\ddot{u}$))× $\mid E/\ddot{u} \mid$. All model predictions are computed at a frequency $f = 1.5\ kHz$.

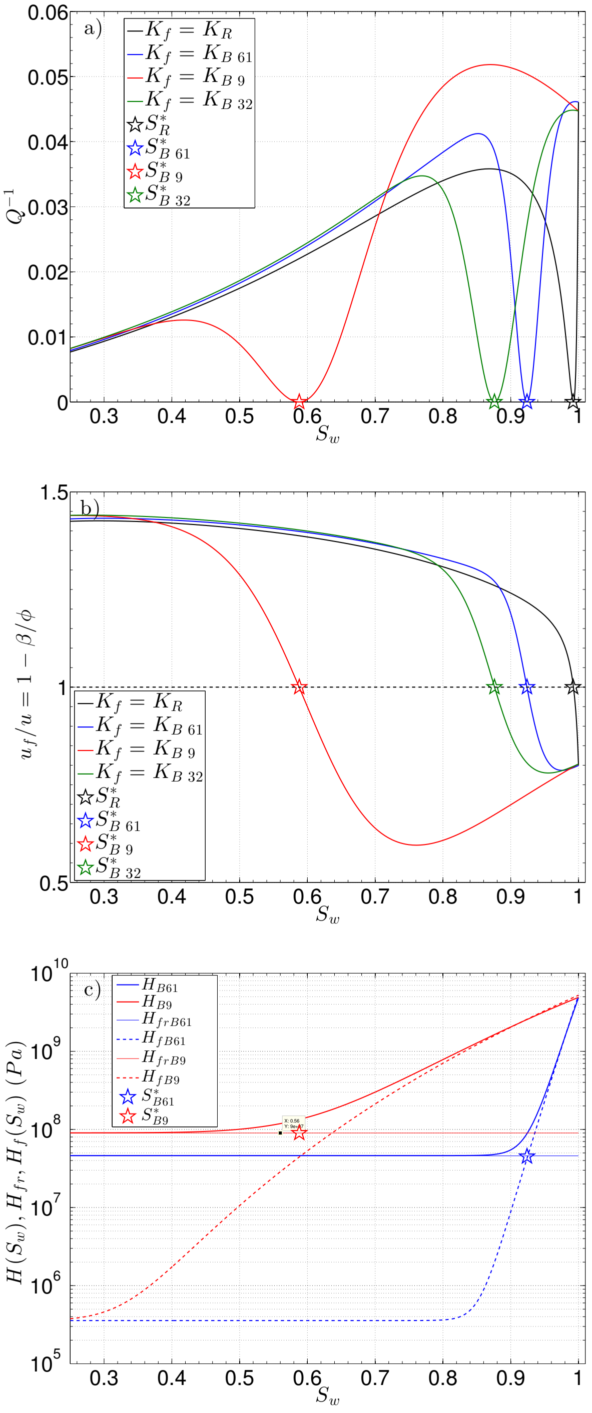

Figure 13. a) Inverse of the seismic quality factor Q^{-1} vs S_w, computed from eq. (1) using properties given in Table 1. Curves are obtained for four distinct estimations of the effective fluid modulus $K_f(S_w)$, as K_R and $K_{B\ e}$ with $e = [9, 32, 61]$. For each case a star, matching the curve in colour, gives the exact location of the critical saturation S^* for which attenuation vanishes. b) Ratio of the fluid over frame displacements $u_f/\ u$ vs saturation S_w. Filtration velocity w is positive when $u_f/u > 1$ and negative when $u_f/u < 1$. The displacements are computed for the same models as in a); note that corresponding critical saturations S^* coincide with $u_f/u = 1$ for which there is no filtration. c) $H(S_w)$, H_{fr} and $H_f(S_w)$ vs S_w computed for two distinct models of effective fluid modulus $K_{B\ 9}$ and $K_{B\ 61}$. Corresponding stars give the exact location of critical saturation S^*.

LIST OF TABLES

1 Properties of the experimental porous medium constituted of Landes sand saturated by a water-gas fluid mixture. The listed parameters are divided into four main classes of properties concerning the fluid, the grain, the frame and the fluid-solid interface. They all intervene within the model computation of the coseismic seismoelectric phenomena presented in eq. (1), a model originally described in Pride & Haartsen (1996), before being extended to partial saturation in Warden et al. (2013) and Bordes et al. (2015). Note that the electrolyte used in this Table is a $NaCl$ solution: for that mixture we used the following relation between conductivity σ_f and concentration C_0 (Haartsen & Pride (1997)): $\sigma_f(C_0) = e^2\,(b_{Na} + b_{Cl})C_0 N_A \times 1000 \simeq C_0 \times 9.3$ where $e = 1.6 \times 10^{-19}$ C is the elementary electric charge, $b_{Na} = b_{Cl} = 3 \times 10^{11}\ m \cdot s^{-1} \cdot N^{-1}$ are the ionic mobilities of cations and anions and $N_A = 6.022 \times 10^{23} mol^{-1}$ is the Avogadro number. The expression of $L(S_w, \omega)$ corresponds to a simplified expression given in Bordes et al. (2015) where $\omega_c(S_w) = 2\pi f_{Biot}(S_w)$, where $f_{Biot}(S_w)$ is the critical pulsation defined upon the properties of the effective fluid.

	Parameter	Notation and units	Values	Comments
Fluid	Water density	$\rho_w\ (kg.m^{-3})$	998	reference water value
	Water viscosity	$\eta_w\ (Pa.s)$	9.91×10^{-4}	Phillips et al. (1978)
	Water permittivity	ϵ_w	80	reference water value
	Water modulus	$K_w\ (Pa)$	2.2×10^9	reference water value
	Conductivity	$\sigma_f\ (mS.m^{-1})$	$[1.7\ -\ 10]$	measured
	Air density	$\rho_g\ (kg.m^{-3})$	1.2	reference air value
	Air viscosity	$\eta_g\ (Pa.s)$	1.8×10^{-5}	reference air value
	Air modulus	$K_g\ (Pa)$	1.5×10^5	reference air value
Effective fluid	Water saturation	S_w	$[0.25\ -\ 1]$	measured
	Residual saturation	S_{w0}	0.25	measured
	Fluid density	$\rho_f\ (kg.m^{-3})$	$\rho_f(S_w) = \rho_g(1-S_w) + \rho_w S_w$	–
	Fluid viscosity	$\eta_f\ (Pa.s)$	$\eta_f(S_w) = \eta_g \left(\frac{\eta_w}{\eta_g}\right)^{S_w}$	Teja & Rice (1981)
Grain	Solid density	$\rho_S\ (kg.m^{-3})$	2650	reference silica value
	Grain modulus	$K_S\ (Pa)$	$3.6 \times 10^{1}0$	reference silica value
Frame	Porosity	ϕ	0.42 ± 0.02	measured
	Permeability	$k_0\ (m^2)$	2×10^{-11}	measured
	Tortuosity	γ_0	1.65 ± 0.15	Holzhauer (2015)
	Bulk modulus	$K_D\ (Pa)$	2.55×10^7	Barrière (2011) from Walton (1987)
			5×10^7	(for drainage and second imbibition)
	Shear modulus	$G\ (Pa)$	1.53×10^7	Barrière (2011) from Walton (1987)
			3×10^7	(for drainage and second imbibition)
	Pore geometry factor	m_P	6	Pride (1994)
	2^{nd} Archie param.	n	2.58	Doussan & Ruy (2009); Bordes et al. (2015)
Fluid-solid interface	Zeta potential	$\zeta\ (mV)$	$0.044 + 0.026\, log[C_0]$	adapted from Pride & Morgan (1991)
	Electrokinetic coef. saturated $C_{ek}(S_w=1) = \frac{\epsilon_0 \epsilon_w \zeta}{\eta_f \sigma_f}$	$C_{ek}\ (V \cdot Pa^{-1})$	$7.14 \times 10^{-7}\ \frac{\zeta(\sigma_f)}{\sigma_f}$	Bordes et al. (2015)
	Electrokinetic coef. $C_{ek}(S_w) = C_{ek}(S_w=1) \times f(S_w)$	–	$f(S_w) = \frac{S_w - S_{w0}}{1 - S_{w0}} S_w^{-n}$	from Jackson (2010) Bordes et al. (2015)
	Static SE coupling coef.	$L_0(S_w)$ $(m^2 \cdot s^{-1} \cdot V^{-1})$	$L_0(S_w) = -\frac{\phi}{\gamma_0}\, \sigma_f S_w^n C_{ek}(S_w)$	from Bordes et al. (2015)
	Dynamic SE coupling coef.	$L(S_w, \omega)$ $(m^2 \cdot s^{-1} \cdot V^{-1})$	$L\,(S_w,\omega) = L_0(S_w) \times \left[1 - i\,\frac{\omega}{\omega_c(S_w)}\,\frac{m_P}{4}\right]^{-1/2}$	from Bordes et al. (2015)

Table 1. Properties of the experimental porous medium constituted of Landes sand saturated by a water-gas fluid mixture. The listed parameters are divided into four main classes of properties concerning the fluid, the grain, the frame and the fluid-solid interface. They all intervene within the model computation of the coseismic seismoelectric phenomena presented in eq. (1), a model originally described in Pride & Haartsen (1996), before being extended to partial saturation in Warden et al. (2013) and Bordes et al. (2015). Note that the electrolyte used in this Table is a $NaCl$ solution: for that mixture we used the following relation between conductivity σ_f and concentration C_0 (Haartsen & Pride (1997)): $\sigma_f(C_0) = e^2\,(b_{Na} + b_{Cl}) C_0 N_A \times 1000 \simeq C_0 \times 9.3$ where $e = 1.6 \times 10^{-19}\ C$ is the elementary electric charge, $b_{Na} = b_{Cl} = 3 \times 10^{11}\ m \cdot s^{-1} \cdot N^{-1}$ are the ionic mobilities of cations and anions and $N_A = 6.022 \times 10^{23} mol^{-1}$ is the Avogadro number. The expression of $L(S_w, \omega)$ corresponds to a simplified expression given in Bordes et al. (2015) where $\omega_c(S_w) = 2\pi f_{Biot}(S_w)$, where $f_{Biot}(S_w)$ is the critical pulsation defined upon the properties of the effective fluid.